



1 **Direct comparisons of ice cloud macro- and microphysical properties**
2 **simulated by the Community Atmosphere Model version 5 with**
3 **HIPPO aircraft observations**

4 Chenglai Wu^{1,2}, Xiaohong Liu^{1,*}, Minghui Diao³, Kai Zhang⁴, Andrew Gettelman⁵,
5 Zheng Lu¹, Joyce E. Penner⁶, and Zhaohui Lin²

6 ¹*Department of Atmospheric Science, University of Wyoming, Laramie, Wyoming,*
7 *USA*

8 ²*International Center for Climate and Environment Sciences, Institute of Atmospheric*
9 *Physics, Chinese Academy of Sciences, Beijing, China*

10 ³*Department of Meteorology and Climate Science, San Jose State University, San*
11 *Jose, California, USA*

12 ⁴*Pacifi Northwest National Laboratory, Richland, Washington, USA*

13 ⁵*National Center for Atmospheric Research, Boulder, Colorado, USA*

14 ⁶*Department of Climate and Space Sciences and Engineering, University of Michigan,*
15 *Ann Arbor, Michigan, USA*

16
17 **Corresponding to:*

18
19 Xiaohong Liu
20 Department of Atmospheric Science
21 University of Wyoming
22 Dept. 3038, 1000 East University Avenue
23 Laramie, WY 82071
24 Email: xliu6@uwyo.edu

25
26
27



28 **Abstract**

29 In this study we evaluate cloud properties simulated by the Community
30 Atmosphere Model Version 5 (CAM5) using in-situ measurements from the HIAPER
31 Pole-to-Pole Observations (HIPPO) for the period of 2009 to 2011. The modeled
32 wind and temperature are nudged towards reanalysis. Model results collocated with
33 HIPPO flight tracks are directly compared with the observations, and model
34 sensitivities to the representations of ice nucleation and growth are also examined.
35 Generally, CAM5 is able to capture specific cloud systems in terms of vertical
36 configuration and horizontal extension. In total, the model reproduces 79.8% of
37 observed cloud occurrences inside model grid boxes, and even higher (94.3%) for ice
38 clouds ($T \leq -40^\circ\text{C}$). The missing cloud occurrences in the model are primarily ascribed
39 to the fact that the model cannot account for the high spatial variability of observed
40 relative humidity (RH). Furthermore, model RH biases are mostly attributed to the
41 discrepancies in water vapor, rather than temperature. At the micro-scale of ice clouds,
42 the model captures the observed increase of ice crystal mean sizes with temperature,
43 albeit with smaller sizes than the observations. The model underestimates the
44 observed ice number concentration (N_i) and ice water content (IWC) for ice crystals
45 larger than $75 \mu\text{m}$ in diameter. Modeled IWC and N_i are more sensitive to the
46 threshold diameter for autoconversion of cloud ice to snow (D_{cs}), while simulated ice
47 crystal mean size is more sensitive to ice nucleation parameterizations than to D_{cs} .
48 Our results highlight the need for further improvements to the sub-grid RH variability
49 and ice nucleation and growth in the model.



50 1 Introduction

51 Cirrus clouds, the type of clouds composed of ice crystals, are one of the key
52 components in the climate system. Cirrus clouds cover about 30% of the globe (Wang
53 et al., 1996; Wylie and Menzel, 1999). They have a significant impact on the earth's
54 radiation balance via two different effects: scattering and reflecting the incoming
55 short wave solar radiation back to space, which leads to a cooling effect on the planet;
56 and absorbing and re-emitting terrestrial longwave radiation, leading to a warming
57 effect (Liou, 1986; Ramanathan and Collins, 1991; Corti et al., 2005). The net
58 radiative effect is thus a balance of these two effects and mainly depends on the
59 amount, microphysical and optical properties of cirrus clouds (Kay et al., 2006;
60 Fusina et al., 2007; Gettelman et al., 2012; Tan et al., 2016). Furthermore, as the
61 efficiency of dehydration at the tropical tropopause layer is strongly influenced by the
62 microphysical processes within cirrus clouds, cirrus clouds can also regulate the
63 humidity of air entering the stratosphere and are recognized as an important
64 modulator for water vapor in the upper troposphere and the lower stratosphere
65 (Gettelman et al., 2002; Wang and Penner, 2010; Jensen et al., 2013; Dinh et al.,
66 2014).

67 Despite their important role in the climate system, there are still large
68 uncertainties in the representation of cirrus clouds in global climate models (GCMs)
69 (Boucher et al., 2013). The uncertainties are the result of several different aspects.
70 First, our understanding of processes initiating the cirrus cloud formation is still
71 limited (DeMott et al., 2003; Kärcher and Spichtinger, 2009; Hoose and Möhler,



72 2012). Ice crystals can form via the homogeneous nucleation of soluble aerosol
73 particles and the heterogeneous nucleation associated with insoluble or partly
74 insoluble aerosol particles (e.g., Hagg et al., 2003; Liu and Penner, 2005; Wang and
75 Liu, 2014). Homogeneous nucleation generally requires higher ice supersaturation
76 and occurs at temperatures colder than about -37°C . It can be fairly well represented
77 by nucleation theory based on laboratory results (Koop et al., 2000). Heterogeneous
78 nucleation is initiated by certain types of aerosols (e.g., mineral dust and biological
79 aerosols) that act as ice nucleating particles (INP), which can nucleate ice particles at
80 significantly lower ice supersaturations in the environment. Currently there are still
81 large unknowns about the types of aerosol, modes of action (e.g.,
82 immersion/condensation, deposition, contact), and the efficiencies of heterogeneous
83 nucleation in the atmosphere (Hoose and Möhler, 2012). Other ice microphysics (e.g.,
84 ice aggregation, deposition/sublimation, and sedimentation), as well as interactions
85 among cirrus microphysical properties, macroscopic properties (e.g., spatial extent),
86 and meteorological fields could further render the interpretation of observed ice cloud
87 properties challenging (Diao et al., 2013; Krämer et al., 2016).

88 In addition to our limited understanding of ice microphysical processes, it is
89 difficult for GCMs with coarse spatial resolution (e.g., tens to hundreds of kilometers
90 in the horizontal direction, and a kilometer in the vertical) to capture the sub-grid
91 variability of dynamical and microphysical processes that are vital for ice cloud
92 formation and evolution. The observed microphysical properties of cirrus clouds vary
93 significantly in time and space (e.g., Hoyle et al., 2005; Diao et al., 2013; Jensen et al.,



94 2013; Diao et al., 2014a), associated with variability in relative humidity, temperature,
95 and vertical wind speed. The spatial extent of clouds is represented in GCMs by
96 diagnosing the cloud fraction in individual model grid boxes using a parameterization.
97 Such a cloud fraction representation needs to be validated with observations in order
98 to identify model biases and to elucidate the reasons behind these biases for future
99 model improvement.

100 Two types of observational data are currently available for validating modeled
101 cirrus cloud properties: in-situ aircraft measurements (e.g., Krämer et al., 2009;
102 Lawson et al., 2011; Diao et al., 2013), and remote-sensing data from space-borne or
103 ground-based instruments (Mace et al., 2005; Deng et al., 2006, 2008; Li et al., 2012).
104 Remote-sensing data may not be directly comparable to model simulations due to the
105 sampling and algorithmic differences between GCM results and remote-sensing
106 retrievals unless a proper simulator, i.e. a so called “satellite simulator”, is adopted
107 (Bodas-Salcedo et al., 2011; Kay et al., 2012). In-situ aircraft observations can
108 provide direct measurements of ice crystal properties such as ice crystal number
109 concentration and size distribution. In particular, these observations are a good source
110 of accurate and fast measurements, and thus provide a unique tool for constraining
111 GCM cirrus parameterizations (e.g., Zhang et al., 2013; Eidhammer et al., 2014).
112 However, the grid scales of GCMs are much larger than those sampled by in-situ
113 observations. Thus direct comparisons at model grid scales are often hindered unless
114 in-situ observations are adequately distributed within the grid boxes and can be scaled
115 up. At the micro-scale level of cirrus clouds (sub-grid scale), statistical comparisons



116 between model simulations and in-situ observations, especially in terms of
117 relationships among cloud microphysical and meteorological variables, are desirable
118 to provide a reliable evaluation of model microphysics (e.g., Zhang et al., 2013;
119 Eidhammer et al., 2014). In addition, aircraft measurements are often limited in their
120 spatial and temporal coverage, which in some sense limits the scope of
121 model-observation comparisons that can be conducted.

122 Previous studies have focused on the evaluation of cirrus clouds from
123 free-running GCM simulations against in-situ observations (e.g., Wang and Penner,
124 2010; Zhang et al., 2013; Eidhammer et al., 2014). However, since the model
125 meteorology was not constrained by conditions that were representative of the time of
126 the observations, the model biases could not be exclusively ascribed to errors in the
127 cirrus parameterizations. Recently, a nudging technique has been developed to allow
128 the simulated meteorology to be more representative of global reanalysis/analysis
129 fields, and thus the comparison between model simulations and observations is more
130 straightforward for the interpretation and attribution of model biases (Kooperman et
131 al., 2012; Zhang et al., 2014). In such simulations, as the meteorology (winds and
132 temperatures) in the GCM are synchronized with observed meteorology, direct
133 comparisons can be achieved by selecting model results that are collocated with
134 observations in space and time, and thus the model outputs can be evaluated in a more
135 rigorous manner.

136 In this study, we use the in-situ aircraft measurements from the NSF HIAPER
137 Pole-to-Pole Observations (HIPPO) campaign (Wofsy et al., 2011) to evaluate the



138 cloud properties simulated by the Community Atmosphere Model version 5 (CAM5).
139 During the HIPPO campaign, high-resolution (~230 m, 1Hz) and comprehensive
140 measurements of ambient environmental conditions (such as air temperature, pressure
141 and wind speed), cloud ice crystals and droplets were obtained. HIPPO also provides
142 a nearly pole-to-pole spatial coverage and relatively long flight hours (~400 hours in
143 total) in various seasons, making it a valuable dataset for GCM evaluations. To
144 facilitate the evaluation, CAM5 is run with specified dynamics where the model
145 meteorological fields (horizontal winds (U, V) and temperature (T)) are nudged
146 towards the NASA GEOS-5 analysis, while water vapor, cloud hydrometeors and
147 aerosols are calculated interactively by the model (Lamarque et al., 2012). Moreover,
148 we select collocated CAM5 output along the HIPPO aircraft flight tracks, and
149 compare the model simulations and observations directly. Our comparisons focus on
150 cloud occurrence, and cloud microphysical properties (e.g., ice water content, number
151 concentration and size distribution of ice particles) with a specific focus on cirrus
152 clouds. We also investigate the sensitivities of model simulated cirrus cloud properties
153 to the ice microphysics parameterizations as well as to the large scale forcing
154 associated with the nudging strategy.

155 The remainder of the paper is organized as follows. In section 2, we introduce the
156 HIPPO observational dataset and instrumentations. The model simulations and
157 experimental design are described in section 3. In section 4, we examine the model
158 performance in simulating cirrus cloud occurrence and microphysical properties and
159 investigate the reasons behind the model biases. Sensitivities of model results to



160 different nudging strategies are presented in section 5, and discussions and
161 conclusions in section 6.

162

163 **2 HIPPO aircraft observations**

164 The NSF HIPPO Global campaign provided comprehensive observations of
165 clouds and aerosols from 87°N to 67°S over the Pacific region during 2009 to 2011
166 (Wofsy et al., 2011). Observations were acquired using the National Science
167 Foundation's Gulfstream V (GV) research aircraft operated by the National Center for
168 Atmospheric Research (NCAR). During this three-year period, five HIPPO
169 deployments were carried out, with each deployment lasting from 23 days to about
170 one month. In total, the HIPPO campaign included 64 flights, 787 vertical profiles
171 (from the surface to up to 14 km), and 434 hours of high-rate measurements
172 (<http://hippo.ucar.edu>). In this study, we use the 1-Hz in-situ measurements of water
173 vapor, temperature, number concentration and size distribution of ice crystals as well
174 as the number concentration of cloud liquid droplets from HIPPO#2-5. HIPPO#1 did
175 not have ice probes onboard.

176 Water vapor was measured by the 25 Hz, open-path Vertical Cavity Surface
177 Emitting Laser (VCSEL) hygrometer (Zondlo et al., 2010). The accuracy and
178 precision of water vapor measurements was ~6% and $\leq 1\%$, respectively.
179 Temperature (T) was recorded by the Rosemount temperature probe. The accuracy
180 and precision of T measurements was 0.5 K and 0.01 K, respectively. Here saturation
181 vapor pressure is calculated following Murphy and Koop (2005), who stated that all



182 the commonly used expressions for the saturation vapor pressure over ice are within 1%
183 in the range between 170 and 273 K. Then we calculate relative humidity (RH) using
184 the saturation vapor pressure with respect to water ($T > 0^\circ\text{C}$) or with respect to ice
185 ($T \leq 0^\circ\text{C}$). Unless explicitly stated otherwise, we refer to RH with respect to water
186 when $T > 0^\circ\text{C}$ and RH with respect to ice when $T \leq 0^\circ\text{C}$.

187 Ice crystal concentrations were measured by the two-dimensional cloud particle
188 imaging (2DC) ice probe (Korolev et al., 2011). The 2DC measures ice crystals with a
189 64-diode laser array at 25 μm resolution and the corresponding size range of 25 –
190 1600 μm . Outside this range, ice crystals between 1600 μm and 3200 μm are
191 mathematically reconstructed. A quality control was further applied to filter out the
192 particles with sizes below 75 μm in order to minimize the shattering effect and optical
193 uncertainties associated with 2DC data. Thus the number concentration (N_i) of ice
194 crystals with diameter from 75 μm to 3200 μm (binned by 25 μm) was derived and is
195 used here for model comparisons. The ice water content (IWC) is derived by
196 integrating the ice crystal mass at each size bin. Mass is calculated from diameter and
197 N_i using the mass-dimension (m - D) relationship of Brown and Francis (1995). For the
198 ice crystal size distribution, a gamma function is assumed as in CAM5 (Morrison and
199 Gettelman, 2008):

$$200 \quad \phi(D) = N_0 D^\mu \exp(-\lambda D) \quad (1)$$

201 where D is diameter, N_0 is the intercept parameter, μ is the shape parameter which is
202 set to 0 currently, and λ is the slope parameter. The slope and intercept for the
203 observed ice crystal size distributions are obtained by fitting Eq. (1) using the least



204 squares method as described in Heymsfield et al. (2008). Observed size distributions
205 that provided less than five bins of non-zero concentrations are not considered in
206 order to maintain a reasonable fit, which is similar to what was done in Eidhammer et
207 al. (2014). This removes about 8% of the total 1-Hz observations of ice clouds
208 ($T \leq -40^\circ\text{C}$). Furthermore, we only retain those fitted size distributions that are well
209 correlated with the measured ones, i.e., with a correlation coefficient larger than 0.6,
210 which leads to a further removal of 10% of the total 1-Hz ice crystal measurements.
211 Note that these screenings are applied only for the derivation of the slope and
212 intercept parameters for the ice crystal size distribution.

213 The cloud droplet number concentration (N_d) was measured by the Cloud Droplet
214 Probe (CDP) during the HIPPO campaign. The CDP measurement range of cloud
215 droplet diameter is 2-50 μm . Because 2DC and CDP probes may report both ice
216 crystals and liquid droplets, we adopted a rigorous criteria for the detection of clouds
217 in different temperature ranges. 99% of the observed N_i are greater than 0.1 L^{-1} , thus a
218 threshold of 0.1 L^{-1} is used to define in-cloud conditions. For $T \leq -40^\circ\text{C}$, we use the
219 criterion of $N_i > 0.1 \text{ L}^{-1}$ to detect the occurrence of ice clouds; For $T > -40^\circ\text{C}$, the
220 occurrence of clouds including mixed-phase clouds ($-40^\circ\text{C} < T \leq 0^\circ\text{C}$) and warm
221 clouds ($T > 0^\circ\text{C}$) are defined by the conditions of either $N_i > 0.1 \text{ L}^{-1}$ or $N_d > 1 \text{ cm}^{-3}$. Here,
222 we only analyze CDP measurements with $N_d > 1 \text{ cm}^{-3}$ to avoid measurement noise as
223 determined by the sensitivity of the instrument.

224 The HIPPO dataset has been previously used for statistical analyses of ice cloud
225 formation conditions and microphysical properties, such as the conditions of the



226 birthplaces of ice clouds – the ice supersaturated regions, the evolutionary trend of
227 RH and N_i inside cirrus clouds, and hemispheric differences in these cloud properties
228 (Diao et al., 2013; 2014a, b). In this study, we will use these observations to evaluate
229 CAM5 simulation of ice clouds. We use 10-second averaged measurements (~ 2.3 km
230 horizontal resolution) which are derived from 1 Hz (~ 230 m horizontal resolution)
231 observations. Although variations are found (mostly within a factor of 2 and
232 sometimes up to 2-3 for N_i , IWC and λ) within 10-second intervals, the 10-second
233 averaged observations shown in this study are similar to those based on 1-second
234 measurements.

235

236 **3 Model and experiment design**

237 **3.1 Model**

238 This study uses version 5.3 of CAM5 (Neale et al., 2012), the atmospheric
239 component of NCAR Community Earth System Model (CESM). The cloud
240 macrophysics scheme in CAM5 provides an integrated framework for treatment of
241 cloud processes and imposes full consistency between cloud fraction and cloud
242 condensates (Park et al., 2014). Deep cumulus, shallow cumulus, and stratus clouds
243 are assumed to be horizontally distributed in each grid layer without overlapping with
244 each other. Liquid stratus and ice stratus are assumed to have a maximum horizontal
245 overlap with each other. Stratiform microphysical processes are represented by a
246 two-moment cloud microphysics scheme (Morrison and Gettelman et al., 2008;
247 hereafter as version 1 of MG scheme (MG1)). MG1 was improved by Gettelman et al.



248 (2010) to allow the ice supersaturation. It is coupled with a modal aerosol model
249 (MAM, Liu et al. (2012a)) for aerosol-cloud interactions. Cloud droplets can form via
250 the activation of aerosols (Abdul-Razzak and Ghan, 2000). Ice crystals can form via
251 the homogeneous nucleation of sulfate aerosol, and/or heterogeneous nucleation of
252 dust aerosol (Liu and Penner, 2005; Liu et al., 2007). The moist turbulence scheme is
253 based on Bretherton and Park (2009). Shallow convection is parameterized following
254 Park and Bretherton (2009), and deep convection is treated following Zhang and
255 McFarlane (1995) with further modifications by Richter and Rasch (2008).

256 Compared to the default version 5.3, the CAM5.3 version we use includes version
257 2 of the MG scheme (MG2) as described by Gettelman and Morrison (2015) and
258 Gettelman et al. (2015). MG2 added prognostic precipitation (i.e., rain and snow) as
259 compared with the diagnostic precipitation in MG1. Note that current version of MG
260 scheme treats cloud ice and snow as different categories with their number and mass
261 predicted, respectively (Morrison and Gettelman, 2008). To be consistent with the
262 observations, here the number and mass concentrations of cloud ice and snow are
263 combined together to get the slope parameter λ following Eidhammer et al. (2014).

264 **3.2 Experimental design for model-observation comparisons**

265 Model experiments are performed using specified dynamics, that is, online
266 calculated meteorological fields (U, V, and T) are nudged towards the GEOS-5
267 analysis (the control experiment, referred to as CTL hereafter), while water vapor,
268 hydrometeors and aerosols are calculated online by the model itself (Lamarque et al.,
269 2012). We also conduct two experiments where only U and V are nudged (referred to



270 as NUG_UV) and with nudging U, V, T and water vapor (Q) (referred to as
271 NUG_UVTQ). These results will be discussed in section 5. The model horizontal and
272 vertical resolutions are $1.9^\circ \times 2.5^\circ$ and 56 vertical levels, respectively. The time step
273 is 30 min. The critical threshold diameter for autoconversion of cloud ice to snow (D_{cs})
274 was found to be an important parameter affecting ice cloud microphysics (e.g., Zhang
275 et al., 2013; Eidhammer et al., 2014). D_{cs} is set to 150 μm in MG2. We also conduct
276 two sensitive experiments using a value of 75 μm (referred to as DCS75) and 300 μm
277 (referred to as DCS300) for D_{cs} (Table 1).

278 In the standard CAM5 model, homogeneous nucleation takes place on sulfate
279 aerosol in the Aitken mode with diameter greater than 0.1 μm (Gettelman et al., 2010).
280 We conduct a sensitivity experiment (referred to as SUL) by removing this size limit
281 (i.e., using all sulfate aerosol particles in the Aitken mode for homogeneous
282 nucleation). Recently, Shi et al. (2015) incorporated the effects of pre-existing ice
283 crystals on ice nucleation in CAM5, simultaneously removing the lower limit of
284 sulfate aerosol size and the upper limit of the sub-grid updraft velocity used for the ice
285 nucleation parameterization. Here a sensitivity experiment (referred to as PRE-ICE)
286 with the Shi et al. (2015) modifications is conducted (Table 1).

287 We run the model from June 2008 to December 2011 (i.e., 43 months) with the
288 first seven months as the model spin-up. For direct comparisons between model
289 results and observations, only model output collocated with HIPPO aircraft flights are
290 recorded. That is, we locate the model grid boxes in which the HIPPO aircraft was
291 transecting through, and then output the model results of these grid boxes at the



292 closest time stamps with respect to the flight time. In total, we have 130,577 in-situ
293 observation samples at 10-second resolution (~363 hours) for HIPPO#2-5. We note
294 that because the current CAM5 model cannot explicitly resolve the spatio-temporal
295 variability of dynamic fields and cloud properties inside a model grid box, there are
296 inevitably certain caveats in its comparison with in-situ observations. For example, as
297 the model time step is 30 min and horizontal grid spacing is ~200 km, there may be
298 cases where tens to hundreds of flight samples are located within one grid box at a
299 specific time stamp. In this study, we find that there are 1 to 170 observation samples
300 within a model grid box. Therefore, we may over-sample the model results within a
301 model grid box with multiple aircraft samples. However, we note that because of the
302 specific flight plan of the HIPPO campaign, most of the HIPPO flights were designed
303 to follow a nearly constant direction when flying from one location to the next, and
304 one vertical profile was generally achieved by about every 3 latitudinal degrees. This
305 unique flight pattern combined with the comparatively long flight hours helps to
306 provide a large amount of observation samples transecting through various climate
307 model grid boxes. In total, 635 model grid boxes are used in the direct comparisons
308 with observations. Considering that the actual horizontal area fraction of a model grid
309 box that the aircraft transected through is relatively small, derivations of grid-scale
310 mean observations which can represent the realistic characteristics for the whole grid
311 box are not possible. Nevertheless, we also derive the mean of observations within a
312 model grid box and compare them with model simulations, and the comparison results
313 are similar to those shown in Section 4. Note that vertical interpolation is taken to



314 account for the altitude variation of model variables for the direct comparison with
315 aircraft observations.

316

317 **4 Results**

318 **4.1 Cloud occurrence**

319 In this section, we will first demonstrate the model performance in simulating the
320 spatial distributions of clouds with a case study. Then we will show the overall
321 features of cloud occurrence for all comparison samples. To identify the reasons for
322 the model-observation discrepancies, we will analyze the meteorology conditions (e.g.,
323 T, Q and RH) and physics processes associated with the formation of clouds. The
324 probability density function (PDF) of ice supersaturation at clear-sky and inside ice
325 clouds will be examined.

326

327 **4.1.1 Case study – a specific cloud system**

328 During HIPPO deployment #4 and research flight 05, the GV aircraft flew from
329 the Cook Islands to New Zealand over the South Pacific Ocean on June 25–26, 2011
330 (Figure 1). Low-level clouds existed along almost all the flight tracks at 700–1000
331 hPa, and most of them were warm clouds ($T > 0^{\circ}\text{C}$). Mid-level (at 400–700 hPa) and
332 high-level clouds (at 250–400 hPa) were also observed. Generally the model captures
333 well the locations of cloud systems along the flight tracks on June 25, 2011. The
334 simulated ice clouds are located above liquid clouds and extend for thousands of
335 kilometers, which corresponds with the observed mid- to high-level clouds at



336 250–600 hPa at UTC 2200–2400 on June 25, 2011. However, the model misses the
337 low-level clouds observed on late June 25 and early June 26, and simulates a smaller
338 horizontal extent for the mid-level cloud at UTC 0230 on June 26. Overall, the
339 observed clouds on June 26 (further South) were more scattered than those on June 25.
340 The model is less capable of reproducing these scattered clouds. CAM5 is better able
341 to simulate cloud systems with larger spatial extents, since these systems are
342 controlled by the nudged large-scale meteorology.

343 Figure 2 shows the time series of RH, Q and T during the flight segment shown in
344 Figure 1. The observations show large spatial variability in RH even during the
345 horizontal flights on June 26. Overall, the simulated RH is within the range of the
346 observations but the model is unable to simulate the larger variability, which occurred
347 on sub-grid spatial scales. Both observed and simulated RH values are above 100%
348 when the model captures the clouds successfully at UTC 2240-2250 and 2310-2330
349 on June 25 and at UTC 0000-0010 on June 26 (denoted by green vertical bars),
350 although the simulated maximum grid-mean RH value is around 110%, which is
351 10-30% less than observed RH values. However, the model cannot capture some of
352 the observed clouds with large RH values within the grid boxes. For example, the
353 model misses the RH associated with low-level clouds (Figure 1) at UTC 2250-2310
354 when simulated grid-mean RH values are around 90% compared to observed values
355 of around 100%. Note that since the aircraft sampled only portions of the model grid
356 boxes, the “over-production” of cloud occurrences by the model shown in Figure 2
357 (blue vertical bars) may not necessarily be the case. Thus we will focus on the cases



358 when the model captures or misses the observed clouds within the model grid boxes.

359 The spatial distributions of RH play an important role in determining whether
360 modeled clouds occur at the same times and locations as those observed. Biases in
361 either Q or T may lead to discrepancies in RH (Figs. 2d and 2f). For example, at
362 around UTC 2150 on June 25, higher RH in the model is caused by the larger
363 simulated Q; at UTC 2250 on June 25, simulated lower RH is mainly caused by the
364 warmer T. To illustrate whether T or Q biases are the main cause for the RH biases,
365 we calculate the offline distribution of RH by replacing the modeled Q or T with the
366 aircraft observations, as shown in Figures 3a and 3b, respectively. After adopting the
367 observed T spatial distributions, the updated RH still misses the RH variability around
368 UTC 0230 – 0400 on June 26, while by adopting the observed Q spatial distribution,
369 the updated RH distribution is very close to the observed one. Thus, in this case study
370 the lack of a large RH spatial variability shown in the observations mainly results
371 from the model's lack of sub-grid scale variability of Q rather than that of T.

372 **4.1.2 Synthesized analyses on cloud occurrences and cloud fraction**

373 The overall performance of the model in simulating the cloud occurrences for all
374 flights in HIPPO 2–5 is shown in Table 2. In the model, clouds often occupy a
375 fraction of a grid box, and cloud fraction together with in-cloud liquid/ice number
376 concentrations are used to represent the occurrence of stratus clouds (Park et al.,
377 2014). For HIPPO, the occurrence of clouds is derived by combining the observations
378 of both liquid and ice number concentrations as described in section 2. In total, the
379 model captures 79.8% of observed cloud occurrences inside model grid boxes. For



380 different cloud types, the model reproduces the highest fraction (94.3%) of observed
381 ice clouds, and the second highest fraction (86.1%) for mixed-phase clouds. In
382 contrast, the model captures only about half (49.9%) of observed warm clouds. As
383 depicted in the case study in section 4.1.1, the missing of cloud occurrences are
384 mainly due to the insufficient representation of sub-grid variability of RH in the
385 model. Next we will further quantify the contribution of sub-grid water vapor and
386 temperature variations to sub-grid variability of RH.

387 **4.1.3 Decomposition of relative humidity biases**

388 The formation of liquid droplets/ice crystals depends on dynamical and
389 thermodynamical conditions such as temperature, water vapor and updraft velocity
390 (Abdul-Razzak and Ghan, 2000; Liu et al., 2007, 2012b; Gettelman et al., 2010). The
391 fraction of liquid/ice stratus clouds is calculated empirically from the grid-mean RH
392 (Park et al., 2014). Thus RH is an important factor for both model representations of
393 cloud occurrences and cloud fraction. RH is a function of pressure, temperature and
394 water vapor. Since we only compare observations with the simulation results on the
395 same pressure levels, differences of RH (dRH) between simulations and observations
396 (i.e., model biases in RH) only result from the differences in temperature and water
397 vapor. We calculate the contributions of biases in water vapor and temperature to the
398 biases in RH following the method that was used to analyze RH spatial variability in
399 Diao et al. (2014a). RH_o (observations) and RH_m (model results) are calculated as:

$$400 \quad RH_m = \frac{e_m}{e_{s,m}}, \quad RH_o = \frac{e_o}{e_{s,o}} \quad (2)$$

401 where e_o and e_m are observed and simulated water vapor partial pressure, respectively,



402 and $e_{s,o}$ and $e_{s,m}$ are observed and simulated saturation vapor pressure over ice ($T \leq 0^\circ\text{C}$)
403 or over water ($T > 0^\circ\text{C}$) in the observations or the model, respectively.

404 Here dRH is calculated from the difference of simulated grid-mean RH (with
405 vertical variances taken into account by the vertical interpolation) and in-situ
406 observations. We define $de = (e_m - e_o)$, and $d(\frac{1}{e_s}) = \frac{1}{e_{s,m}} - \frac{1}{e_{s,o}}$, therefore dRH is

$$407 \quad dRH = RH_m - RH_o = de \cdot \frac{1}{e_{s,o}} + e_o \cdot d(\frac{1}{e_s}) + de \cdot d(\frac{1}{e_s}) \quad (3)$$

408 Thus dRH can be separated into three terms: the first term is the contribution from the
409 water vapor partial pressure (dRH_q), the second term from temperature (dRH_T), and
410 the third term for concurrent impact of biases in temperature and water vapor
411 ($dRH_{q,T}$).

412 Figure 4 shows the contributions of these three terms to dRH for different
413 temperature ranges. All the three terms as well as dRH are given in percentage. The
414 intercepts and slopes of linear regression lines for dRH_q versus dRH , dRH_T versus
415 dRH , and $dRH_{q,T}$ versus dRH are also presented. As temperature is constrained by
416 GEOS-5 analysis, the bias in temperature is reduced (although not eliminated) to
417 mostly within $\pm 7^\circ\text{C}$. A considerable amount of discrepancy in RH exist between
418 model and observations. The model successfully captures the clouds (green symbols)
419 when the simulated RH is close to observations in all the three temperature ranges.
420 The model tends to miss the clouds (red symbols) when lower RH is simulated, and
421 produces spurious clouds (blue symbols) when higher RH is simulated. Regarding the
422 contributions of dRH_q and dRH_T to dRH , the slopes of the linear regression for dRH_q



423 versus dRH are 0.748, 0.933 and 0.786 for $T \leq -40^\circ\text{C}$, $-40^\circ\text{C} < T \leq 0^\circ\text{C}$ and $T > 0^\circ\text{C}$,
424 respectively, which are much larger than those for dRH_T versus dRH (0.087, 0.072
425 and 0.210 for the three temperature ranges, respectively). This indicates that most of
426 the biases in RH are contributed by the biases in water vapor (dRH_q). However, for
427 $T > 0^\circ\text{C}$, although dRH_q still dominates, dRH_T contributes notably to 21% of the RH
428 biases. For $T \leq -40^\circ\text{C}$, $dRH_{q,T}$ also contributes about 17% to dRH , indicating
429 concurrent impact from biases of T and water vapor. In contrast, for $-40^\circ\text{C} < T \leq 0^\circ\text{C}$
430 and $T > 0^\circ\text{C}$, the contributions of $dRH_{q,T}$ to dRH are negligible. We note that the slopes
431 of linear regression lines for dRH_q versus dRH and dRH_T versus dRH indicate the
432 average contributions from water vapor and temperature biases to the RH biases,
433 respectively. The values of dRH_T can occasionally reach up to $\pm 100\%$, which
434 suggests the large impact from temperature biases in these cases. In addition, the
435 dRH_T and dRH_q terms can have the same (opposite) signs, which would lead to larger
436 (lower) total biases in RH. The coefficients of determination, R^2 , for the linear
437 regressions indicate that dRH_q versus dRH has a much stronger correlation than that
438 of dRH_T versus dRH .

439 4.1.4 Ice supersaturation

440 Ice nucleation only occurs in the regions where ice supersaturation exists.
441 Different magnitudes of ice supersaturation are required to initiate homogeneous and
442 heterogeneous nucleation (Liu and Penner, 2005). The distribution of ice
443 supersaturation may provide insights into the mechanisms for ice crystal formation
444 (e.g., Haag et al., 2003). In CAM5, ice supersaturation is allowed (Gettelman et al.,



445 2010). Homogeneous nucleation occurs when $T \leq -35^\circ\text{C}$ and ice supersaturation
446 reaches a threshold ranging from 145% to 175%. Dust aerosol can serve as INPs
447 when $\text{RH} > 120\%$. Ice supersaturation will be relaxed back to saturation via the vapor
448 deposition process (Liu et al., 2007; Gettelman et al., 2010).

449 To examine the discrepancies in ice supersaturation between model results and
450 observations, we compare the distribution of RH for conditions in clear-sky and
451 within cirrus clouds (Figure 5). The analysis is limited to the conditions of $T \leq -40^\circ\text{C}$
452 for both model simulations and observations. In CAM5, RH diagnosed in different
453 sections of the time integration procedure can be different due to the time splitting
454 algorithm. We present here both the RH before and after the microphysical processes.

455 The observations show that ice supersaturation exists in both clear-sky and
456 inside-cirrus conditions. In clear-sky environments, the PDF of RH shows a
457 continuous decrease with RH values in subsaturated conditions, followed by a
458 quasi-exponential decrease with the RH above saturation. The maximum RH_i reaches
459 up to 150%. In cirrus clouds, most of RH values range from 50% to 150% with a peak
460 in the PDF near 100%. This feature is consistent with the results of Diao et al. (2014b),
461 who used 1-second HIPPO measurements and separated the southern and the northern
462 hemispheres for comparison.

463 The PDFs of modeled RH before and after the microphysical processes are very
464 similar except the latter one has slightly lower probability of RH_i above 140% for
465 inside-cirrus conditions. Compared to the observations, the model can simulate the
466 occurrences of ice supersaturation in both clear-sky and in-cloud conditions. However,



467 inside cirrus clouds, the simulated PDF of RH peaks around 120% instead of 100% as
468 observed. Outside the cirrus clouds (clear-sky), the model simulates a much lower
469 probability of ice supersaturation with the maximum RH value around 120%. The
470 largest ice supersaturation simulated by CAM5 under clear-sky conditions is around
471 20%, which corresponds to the ice supersaturation of 20% assumed in the model for
472 the activation of heterogeneous nucleation. This indicates the dominant mode of
473 heterogeneous nucleation in the model. However, the observations show much higher
474 frequencies of ice supersaturations larger than 20%, indicating higher RH thresholds
475 for homogeneous nucleation or heterogeneous nucleation.

476

477 **4.2 Microphysical properties of ice clouds**

478 Together with cirrus cloud fraction, the ice crystal number concentration and size
479 distribution within cirrus clouds determine the radiative forcing of cirrus clouds. In
480 this section, we will present the evaluation of modeled microphysical properties of
481 cirrus clouds for $T \leq -40^\circ\text{C}$. As measurements of ice crystal number concentration
482 include both ice and snow crystals, for comparison with observations, we combine the
483 cloud ice and snow simulated in the model (hereafter referred as ice crystals).
484 Following Eidhammer et al. (2014), the slope and intercept parameters of the gamma
485 function for the ice crystal size distribution simulated by the model are derived from
486 the total number concentration and mass mixing ratio of cloud ice and snow, which
487 are the integrations of the first and third moments of the size distribution function.
488 The simulated number concentration of ice crystals with sizes larger than $75 \mu\text{m}$ is



489 calculated by the integration of gamma size distributions from 75 μm to infinity. The
490 simulated IWC for ice crystals with sizes larger than 75 μm is also derived by
491 integrating the mass concentration of cloud ice and snow from 75 μm to infinity. We
492 note that about 94% of total cirrus cloud samples are at temperatures between -60°C
493 and -40°C .

494 4.2.1 Ice crystal size distribution

495 Direct comparison of the slope parameter (λ) for ice crystal size distributions is
496 shown in Figure 6. The slope parameter λ determines the decay rate of a gamma
497 function in relation to the increasing diameter. With a larger λ , the decay of a gamma
498 function with increasing size is faster and there are relatively fewer large ice crystals.
499 The number-weighted mean diameter can be defined as the inverse of λ (i.e., λ^{-1}). As
500 shown in Figure 6, the observed λ is generally within the range from 10^3 to 10^5 m^{-1} .
501 The model reproduces the magnitude of λ for some of the observations, but tends to
502 overestimate the observations for smaller λ values (10^3 to 10^4 m^{-1}). This indicates that
503 the model produces higher fractions of ice crystals at smaller sizes, and the
504 number-weighted mean diameter is underestimated. Moreover, the model generally
505 simulates λ in a narrower range of 7.5×10^3 to $7 \times 10^4 \text{ m}^{-1}$ for the three experiments with
506 different D_{es} (CTL, DCS75, DCS300). SUL and PRE-ICE simulate a wider range of λ
507 which is comparable to the observations but tends to shift λ to larger values (5×10^4 to
508 $1 \times 10^5 \text{ m}^{-1}$). All the experiments rarely simulated the occurrence of small λ (below
509 $7.5 \times 10^3 \text{ m}^{-1}$).

510 Figure 7 shows the relationship of λ with temperature from observations and



511 model simulations. Here, both the geometric means and the standard deviations of λ
512 for each temperature interval of 4°C are also shown. Although the observed λ doesn't
513 monotonically decrease with increasing temperature, overall an decreasing trend can
514 be found for the whole temperature range below -40°C. This indicates a general
515 increase in the number-weighted mean diameter of ice crystals with increasing
516 temperature. The correlation between λ and temperature from HIPPO is similar to that
517 from the Atmospheric Radiation Measurements Spring Cloud Intensive Operational
518 Period in 2000 (ARM-IOP) and the Tropical Composition, Cloud and Climate
519 Coupling (TC4) campaigns as shown in Eidhammer et al. (2014), but the HIPPO
520 observations extend to lower temperatures than ARM-IOP and TC4 observations
521 where temperatures are mostly above -56 °C. In addition, HIPPO observations show a
522 broader scatter range of λ , which may be because HIPPO sampled ice crystals at
523 various environment conditions as the flight tracks covered much wider areas and
524 lasted for much longer periods. The decrease of λ with increasing temperature has
525 been shown in many other studies (e.g., Heymsfield et al., 2008; 2013). Such a feature
526 is mainly due to more large ice particles at higher temperatures, and can also be partly
527 explained by more ice crystals formed from nucleation and less water vapor available
528 for ice crystal growth at lower temperatures (Eidhammer et al., 2014).

529 Compared to the observations, the simulated mean λ is about 2-4 times larger for
530 all the experiments, indicating that the model simulates smaller mean sizes for ice
531 crystals. The simulated λ decreases with increasing temperature, which is generally
532 consistent with the observations. In addition, the geometric standard deviations (less



533 than 2) of simulated λ are smaller than observed (around 2-3). This can be partly
534 explained by the fact that in-situ observations sampled the sub-grid variability of
535 cloud properties.

536 The difference of simulated λ is within a factor of 2 among the five experiments
537 when temperature is between -40°C and -56°C , and is larger (around 2-4) when
538 temperature is below -56°C . For the experiments with different D_{cs} , CTL and DCS75
539 simulated λ are close to each other when temperature is between -40°C and -60°C ,
540 and DCS300 simulates larger λ compared to DCS75 and CNTL. For temperatures
541 between -64°C and -72°C , CTL and DCS300 simulated λ are close to each other and
542 both are larger than that of DCS75. For the experiments with different ice nucleation
543 parameterizations, both SUL and PRE-ICE simulate larger λ than CTL especially for
544 temperatures below -56°C . SUL simulates the largest λ of all the experiments. This
545 can be explained by much larger number concentration of ice crystals (for all size
546 range, figure not shown) simulated by SUL, while IWC is not very different from
547 other experiments (section 4.2.3).

548

549 4.2.2 Ice crystal number concentration

550 Figure 8 shows the comparison of in-cloud number concentrations (N_i) of ice
551 crystals with diameters larger than $75\ \mu\text{m}$ between observations and simulations. The
552 magnitude of observed N_i varies by three orders of magnitude from $10^{-1}\ \text{L}^{-1}$ to $10^2\ \text{L}^{-1}$.
553 The model simulates reasonably well the range of N_i in cirrus clouds. However, the
554 model tends to underestimate N_i for all the experiments except DCS75. About 13%



555 (DCS75) to 30% (PRE) of observations are underestimated in the model by a factor of
556 10. The underestimation of N_i may be partly attributed to the fact that the model
557 underestimates the ice crystal size (section 4.2.1), leading to a smaller fraction of ice
558 crystals with diameter larger than 75 μm . Additional bias may result from the bias in
559 the total ice crystal number concentration, although the observations are not available
560 for comparison. We also compare simulated N_i with observed in-cloud N_i averaged
561 within the model grid boxes. We choose the flight segments with over 300 1-second
562 aircraft measurements within an individual model grid and calculate the average for
563 in-cloud N_i of ice clouds ($T \leq -40$ °C). The comparison results are, however, similar to
564 those shown in Figure 8.

565 DCS75 reasonably simulates the occurrence frequency of $N_i < 1 \text{ L}^{-1}$ albeit with
566 significantly higher frequency for N_i around 1-5 L^{-1} and lower frequency for N_i
567 around 5-10 L^{-1} . Most of the experiments cannot reproduce the occurrence frequency
568 of high N_i ($N_i > 50 \text{ L}^{-1}$) except DCS75 and PRE-ICE.

569 The relationships between N_i and temperature are shown in Figure 9. Since N_i
570 here only takes into account of ice crystals larger than 75 μm , the geometric mean of
571 observed N_i generally ranges between 5-10 L^{-1} for temperatures below -40°C, which
572 is 1-2 orders of magnitude lower than the number of ice crystals between 0.3-775 μm
573 from observations compiled by Krämer et al. (2009) and between 10-3000 μm from
574 the SPARTICUS campaign (Zhang et al., 2013), but is comparable to the number of
575 ice crystals in the same size range from the ARM-IOP and TC4 campaigns
576 (Eidhammer et al., 2014). The geometric standard deviation of observed N_i within a



577 temperature interval of 4°C can be as high as a factor of 5.

578 The model simulates no apparent trends of N_i when temperature decreases from
579 -40°C to -60°C for the experiments CTL, DCS75 and PRE-ICE. The model simulates
580 somehow larger N_i with decreasing temperatures for the experiments DCS300 and
581 SUL. Increase of N_i at lower temperatures in SUL may indicate the occurrence of
582 homogeneous nucleation. Overall, simulated N_i is sensitive to D_{cs} . Simulated N_i is
583 also sensitive to the number of sulfate aerosol particles for homogeneous nucleation.
584 With the removal of the lower size limit (0.1 μm diameter) of sulfate aerosol particles
585 for homogeneous nucleation in the experiment SUL, simulated N_i is significantly
586 higher than that in CTL. This result is consistent with that of Wang et al. (2014).

587 Although some experiments can simulate a similar magnitude of N_i as the
588 observations in some temperature ranges, most of the experiments underestimate N_i
589 and some experiments (CTL and PRE-ICE) underestimate N_i for all the temperature
590 ranges. Overall DCS75 simulates the closest magnitude of N_i with the observations
591 for temperatures from -40°C to -64°C.

592

593 4.2.3 Ice water content

594 Figure 10 shows the comparison of in-cloud IWC for ice crystals with diameter
595 larger than 75 μm between observations and simulations. The magnitude of observed
596 IWC varies by four orders of magnitude from 10⁻² to 10² mg m⁻³, which is within the
597 range of observed IWC in previous studies (Kramer et al., 2016; Luebke et al., 2016).
598 Observed IWC here is mostly larger than 1 mg m⁻³. Compared to the observations, the



599 model for all the experiments underestimates observed IWC for 70%-95% of the
600 samples and by one order of magnitude for 25%-45% of the samples. Although the
601 model reproduces the highest occurrence frequency of IWC around $1\text{-}5\text{ mg m}^{-3}$, the
602 model simulates more occurrence of IWC below 1 mg m^{-3} and fewer occurrence of
603 IWC above 5 mg m^{-3} .

604 The relationships between IWC and temperature are shown in Figure 11. An
605 overall increasing trend of observed IWC with temperature is found for the entire
606 temperature range. The observed relationship between IWC and temperature is
607 consistent with those shown in the previous studies (e.g., Kramer et al., 2016; Luebke
608 et al., 2016). However, the mean IWC from HIPPO is 3-5 times as large as previous
609 observations (Kramer et al., 2016; Luebke et al., 2016). Observations here only
610 account for ice crystals with diameter larger than $75\text{ }\mu\text{m}$ and thus it is less frequent
611 that observed IWC is lower than 1 mg m^{-3} . In contrast, previous studies showed that
612 IWC (including smaller sizes of ice crystals) lower than 1 mg m^{-3} was often measured
613 in observations. This contributes to the mean IWC shown here being larger than that
614 in the previous studies.

615 The simulated IWC is lower than observations for all the experiments at
616 temperatures between -40°C and -60°C where most of the observations were made.
617 The model also simulates less variation of IWC with temperature when temperature is
618 between -40°C and -60°C . When temperature is below -60°C , a steep decrease of
619 IWC is found in some experiments (e.g., CTL, SUL). Considering the large scatter of
620 IWC and relatively few samples available, this may be due to a lack of a sufficient



621 number of samples. Therefore, more observations are needed to have a robust
622 comparison for relatively low temperatures (i.e., temperatures below $-60\text{ }^{\circ}\text{C}$).
623 Simulated IWC is more sensitive to D_{cs} than to ice nucleation.

624

625 **5 Impact of Nudging**

626 In previous sections, we have nudged the simulated winds and temperature
627 towards the GEOS5 analysis, but kept the water vapor on-line calculated by the model
628 itself. We showed that the model captures a large portion (79.8%) of cloud
629 occurrences presented in the observations. We also identified the RH bias in the
630 simulation and attributed the RH bias mainly to the bias in water vapor. As the bias in
631 temperature is reduced in the nudging run compared to the free run, the attribution of
632 RH bias in the free-running model (i.e., no nudging applied) is still unclear. To
633 examine the impact of nudging strategies on the cloud occurrences and the attribution
634 of RH bias, we conducted two additional experiments: one with neither temperature
635 nor specific humidity nudged to the analysis (hereafter referred as NUG_UV), and the
636 other one with both temperature and specific humidity nudged to the analysis
637 (hereafter referred as NUG_UVTQ). Without nudging temperature, the model
638 experiment (NUG_UV) has a cold temperature bias of $-1.8\text{ }^{\circ}\text{C}$ on average relative to
639 the HIPPO observations (Figure not shown). In comparison, the temperatures
640 simulated by CTL and NUG_UVTQ are more consistent with in situ aircraft
641 observations, and the mean temperature is slightly underestimated by $0.22\text{ }^{\circ}\text{C}$ and
642 $0.28\text{ }^{\circ}\text{C}$ in these two experiments, respectively. By nudging specific humidity, the



643 model experiment (NUG_UVTQ) improves the simulation of grid-mean water vapor
644 concentrations by eliminating the biases especially for the cases with low water vapor
645 concentrations (less than 20 ppmv, Figure not shown). NUG_UV captures 86.0%,
646 80.9%, and 39.7% of observed ice, mixed-phase, and warm clouds, respectively,
647 which are slightly smaller than those of CTL (i.e., 94.3%, 86.1%, and 49.9%,
648 respectively). For NUG_UVTQ, although 73.5% of ice clouds are captured, the model
649 captures only 61.8% of mixed-phase clouds and 31.4% of warm clouds. The worse
650 simulation in NUG_UVTQ may be because the nudged water vapor is not internally
651 consistent with the modeled cloud physics, which deteriorates the simulation of cloud
652 occurrences.

653 As seen in Table 3, in the two new nudging experiments (NUG_UV and
654 NUG_UVTQ), modeled RH biases in the comparison with in-situ observations also
655 mainly result from the discrepancies of water vapor. The contribution of dRH_q to dRH
656 ranges from 65.8% to 92.5%, which are slightly smaller than those in CTL. In
657 NUG_UV, as the model underestimates the temperature, modeled RH is
658 systematically higher than observations, especially for $T \leq -40^\circ\text{C}$ where the absolute
659 value of RH is overestimated by 30% on average. The large T bias leads to a smaller
660 contribution from the water vapor bias (dRH_q) and a larger contribution from the
661 concurrent bias in temperature and water vapor ($dRH_{q,T}$). When both T and Q are
662 nudged in NUG_UVTQ, the contributions of the three terms to dRH are generally
663 similar to those in CTL. A larger contribution from temperature (dRH_T) is found for
664 temperature above 0°C in NUG_UVTG. This may be a result of smaller contributions



665 from either dRH_q or $dRH_{q,T}$ due to the reduced water vapor bias. We also examined
666 the in-cirrus microphysical properties simulated by these two new nudging
667 experiments. The model features such as underestimations of N_i , IWC, and mean ice
668 crystal size are similar to those in CTL and are not sensitive to the nudging strategy
669 used.

670

671 **6 Discussion and Conclusions**

672 In this study, we evaluated the macro- and microphysical properties of ice clouds
673 simulated by CAM5 using in-situ measurements from the HIPPO campaign. The
674 HIPPO campaign sampled over the Pacific region from 67°S to 87°N across several
675 seasons, making it distinctive from other previous campaigns and valuable for
676 providing insight into evaluating model performance. To eliminate the impact of
677 large-scale circulation biases on the simulated cloud processes, we ran CAM5 using
678 specified dynamics which nudge the simulated meteorology (U, V and T) towards the
679 GEOS-5 analysis while keeping water vapor, hydrometeors, and aerosols online
680 calculated by the model itself. Model results collocated with the flight tracks spatially
681 and temporally are directly compared with the observations. Modeled cloud
682 occurrences and in-cloud ice crystal properties are evaluated, and the reasons for the
683 biases are examined. We also examined the model sensitivity to D_{cs} and different
684 parameterizations for ice nucleation.

685 The model can reasonably capture the vertical configuration and horizontal
686 extension of specific cloud systems. In total, the model captures 79.8% of observed



687 cloud occurrences within model grid boxes. For each cloud type, the model captures
688 94.3% of observed ice clouds, and 86.1% of mixed-phase and 49.9% of warm clouds.
689 This result is only modestly sensitive to whether meteorological fields (T and Q) are
690 nudged. The model cannot capture the large spatial variability of observed RH, which
691 is responsible for much of the model missing of low-level warm clouds. A large
692 portion of the RH bias results from the discrepancy in water vapor, with a small
693 portion from the discrepancy in temperature. The model also underestimates the
694 occurrence frequencies of ice supersaturation higher than 20% under clear-sky
695 conditions (i.e., outside of cirrus clouds), which may indicate too low threshold for
696 initiating heterogeneous ice nucleation in the model. In fact, a study comparing the
697 observed RH distributions with real-case simulations of the Weather Research and
698 Forecasting (WRF) model suggested that the threshold for initiating heterogeneous
699 nucleation should be set at $RH_i \geq 125\%$ (D'Alessandro et al., submitted).

700 Down to the micro-scale of cirrus clouds ($T \leq -40$ °C), the model captures well the
701 decreasing trend of λ with increasing temperature from -72 °C to -40 °C. However, the
702 simulated λ values are about 2-4 times on average larger than observations at all the
703 4°C temperature ranges for all the experiments with different D_{cs} and different ice
704 nucleation parameterizations. This indicates that the model simulates a smaller mean
705 size of ice crystals in each temperature range. The model is mostly able reproduce the
706 magnitude of observed N_i (to within one order of magnitude) for ice crystals with
707 diameter larger than 75 μm , yet generally underestimates N_i except for the DCS75
708 simulation. Simulated N_i is sensitive to D_{cs} and the number of sulfate aerosol particles



709 for homogeneous nucleation used in the model. No apparent correlations between the
710 mean N_i and temperature are found in the observations, while a decrease of N_i with
711 increasing temperature is found in the two simulations (DCS300 and SUL). All the
712 experiments underestimate the magnitude of IWC for ice crystals larger than 75 μm .
713 The observations show an overall decreasing trend of IWC with decreasing
714 temperature while the model simulated trends are not as strong. Simulated IWC is
715 sensitive to D_{cs} but less sensitive to the different parameterizations of ice nucleation
716 examined here.

717 Current climate models have typical horizontal resolutions of tens to hundreds of
718 kilometers and are unable to represent the large spatial variability of environmental
719 conditions for cloud formation and evolution within a model grid box. A previous
720 study of Diao et al. (2014a) shows that the spatial variability of water vapor
721 dominantly contribute to the spatial variability in RH, compared with the
722 contributions from those of temperature. Here our comparisons of model simulations
723 with observations show that the biases in water vapor spatial distributions are the
724 dominant sources of the model biases in RH spatial distributions. Thus it is a priority
725 to develop parameterizations that are able to treat the sub-grid variability of water
726 vapor for climate models. There are also substantial sub-grid variations of cloud
727 microphysical properties shown in previous observational studies (e.g., Lebsock et al.,
728 2013). Currently a framework for treating the sub-grid variability of temperature,
729 moisture and vertical velocity has been developed and implemented into CAM5
730 (Bogenschutz et al., 2013). A multi-scale modeling framework has also been



731 developed to explicitly resolve the cloud dynamics and cloud microphysics down to
732 the scales of cloud-resolving models (e.g., Wang et al., 2011; Zhang et al., 2014). The
733 PDFs of sub-grid scale distributions can be sampled on sub-columns for cloud
734 microphysics (Thayer-Calder et al., 2015). With the increase of model resolutions for
735 future model developments, the subgrid variability of temperature, moisture, and
736 cloud microphysics and dynamics will be better resolved. We plan to evaluate the
737 model performances at higher resolutions.

738 Given the various environmental conditions and aerosol characteristics in the
739 atmosphere, the formation and evolution of ice crystals are not well understood, and it
740 is even more challenging for climate models to represent these processes. For the bulk
741 ice microphysics used in our model, several assumptions have to be made to simulate
742 both N_i and λ . One of them is to partition the ice crystals into cloud ice and snow
743 categories, while using D_{cs} to convert cloud ice to snow. Thus a more physical
744 treatment of ice crystal evolution such as using bin microphysics (e.g., Bardeen et al.,
745 2013; Khain et al., 2015) or a single category to represent all ice-phase hydrometeors
746 (Morrison and Milbrandt, 2015) is needed.

747

748 **Acknowledgements**

749 X. Liu and C. Wu acknowledge support of the U.S. Department of Energy's
750 Atmospheric System Research Program (grant DE-572 SC0014239). The authors
751 would like to acknowledge the use of computational resources (ark:/85065/d7wd3xhc)
752 at the NCAR-Wyoming Supercomputing Center provided by the National Science



753 Foundation and the State of Wyoming, and supported by NCAR's Computational and
754 Information Systems Laboratory. We appreciate the efforts of the National Center for
755 Atmospheric Research (NCAR) Earth Observing Laboratory flight, technical, and
756 mechanical crews during the National Science Foundation (NSF) HIPPO Global
757 campaign, in particular the PIs of the HIPPO Global campaign: S. Wofsy, R. Keeling,
758 and B. Stephens. NCAR is sponsored by NSF. We acknowledge the support of the
759 VCSEL hygrometer by M. Diao, M. Zondlo and S. Beaton, the support of 2DC probe
760 by A. Bansemer, C. J. Webster and D. C. Rogers. We also acknowledge the funding
761 of NSFAGS-1036275 for field support and data analyses from the VCSEL
762 hygrometer in the HIPPO Global campaign. M. Diao gratefully acknowledges the
763 support from the NCAR Advanced Study Program (ASP) postdoctoral fellowship in
764 Oct 2013– Aug 2015. Final data sets and documentation from the NSF HIPPO Global
765 campaign can be accessed at <<http://hippo.ornl.gov>> in the Carbon Dioxide
766 Information Analysis Center Data Archive at Oak Ridge National Laboratory. We
767 thank T. Eidhammer from NCAR for her help on model result analysis.

768

769 **References**

- 770 Abdul-Razzak, H., and Ghan, S. J.: A parameterization of aerosol activation 2.
771 Multiple aerosol types. *J. Geophysical Research-Atmospheres* 105(D5),
772 6837-6844, 2000.
- 773 Bodas-Salcedo, A. et al.: COSP: A satellite simulation software for model assessment.
774 *Bull. Amer. Meteor. Soc.*, 92, 1023–1043, 2011.
- 775 Bardeen, C. G., A. Gettelman, E. J. Jensen, A. Heymsfield, A. J. Conley, J. Delanoë,
776 M. Deng, O. B. Toon (2013), Improved cirrus simulations in a GCM using
777 CARMA sectional microphysics, *J. Geophys. Res.*, 118,
778 doi:10.1002/2013JD020193.
- 779 Bogenschütz, P. A., Gettelman, A., Morrison, H., Larson, V. E., Craig, C., and



- 780 Schanen, D. P.: Higher-Order Turbulence Closure and Its Impact on Climate
781 Simulations in the Community Atmosphere Model, *J Climate*, 26, 9655-9676,
782 10.1175/JCLI-D-13-00075.1, 2013.
- 783 Boucher, O., and Coauthors: Clouds and Aerosols, in: *Climate Change 2013: The*
784 *Physical Science Basis. Contribution of Working Group I to the Fifth*
785 *Assessment Report of the Intergovernmental Panel on Climate Change*, edited by:
786 Stocker, T.F., et al., 1535, 571-657, Cambridge University Press, Cambridge,
787 United Kingdom and New York, NY, USA, 2013.
- 788 Bretherton, C. S., and Park, S.: A New Moist Turbulence Parameterization in the
789 Community Atmosphere Model, *J Climate*, 22, 3422-3448,
790 10.1175/2008JCLI2556.1, 2009.
- 791 Corti, T., Luo, B. P., Peter, T., Vömel, H., and Fu, Q.: Mean radiative energy balance
792 and vertical mass fluxes in the equatorial upper troposphere and lower
793 stratosphere, *Geophys Res Lett*, 32, L06802, 10.1029/2004GL021889, 2005.
- 794 DeMott, P. J., Cziczo, D. J., Prenni, A. J., Murphy, D. M., Kreidenweis, S. M.,
795 Thomson, D. S., Borys, R., and Rogers, D. C.: Measurements of the
796 concentration and composition of nuclei for cirrus formation, *Proceedings of the*
797 *National Academy of Sciences*, 100, 14655-14660, 10.1073/pnas.2532677100,
798 2003.
- 799 Deng, M., and Mace, G. G.: Cirrus Microphysical Properties and Air Motion Statistics
800 Using Cloud Radar Doppler Moments. Part I: Algorithm Description, *Journal of*
801 *Applied Meteorology and Climatology*, 45, 1690-1709, 10.1175/JAM2433.1,
802 2006.
- 803 Deng, M., and Mace, G. G.: Cirrus Microphysical Properties and Air Motion Statistics
804 Using Cloud Radar Doppler Moments. Part II: Climatology, *Journal of Applied*
805 *Meteorology and Climatology*, 47, 3221-3235, 10.1175/2008JAMC1949.1,
806 2008.
- 807 D'Alessandro, J., Diao, M., Wu, C., Liu, X., Chen, M., Morrison, H., Eidhammer, T.,
808 Jensen, Jorgen B. B., Bansemmer, A., Zondlo, M. A. and DiGangi, J. P.: Dynamical
809 conditions of ice supersaturation in convective systems: a comparative analysis
810 between in-situ aircraft observations and WRF simulations, submitted.
- 811 Diao, M., Zondlo, M. A., Heymsfield, A. J., Beaton, S. P., and Rogers, D. C.:
812 Evolution of ice crystal regions on the microscale based on in situ observations,
813 *Geophys Res Lett*, 40, 3473-3478, 10.1002/grl.50665, 2013.
- 814 Diao, M., Zondlo, M. A., Heymsfield, A. J., Avallone, L. M., Paige, M. E., Beaton, S.
815 P., Campos, T., and Rogers, D. C.: Cloud-scale ice-supersaturated regions
816 spatially correlate with high water vapor heterogeneities, *Atmos. Chem. Phys.*,
817 14, 2639-2656, 10.5194/acp-14-2639-2014, 2014a.
- 818 Diao, M., Zondlo, M. A., Heymsfield, A. J., and Beaton, S. P.: Hemispheric
819 comparison of cirrus cloud evolution using in situ measurements in HIAPER
820 Pole-to-Pole Observations, *Geophys Res Lett*, 41, 4090-4099,
821 10.1002/2014GL059873, 2014b.
- 822 Dinh, T., Fueglistaler, S., Durran, D., and Ackerman, T.: Cirrus and water vapour
823 transport in the tropical tropopause layer – Part 2: Roles of ice nucleation and



- 824 sedimentation, cloud dynamics, and moisture conditions, *Atmos. Chem. Phys.*,
825 14, 12225-12236, 10.5194/acp-14-12225-2014, 2014.
- 826 Eidhammer, T., Morrison, H., Bansemer, A., Gettelman, A., and Heymsfield, A. J.:
827 Comparison of ice cloud properties simulated by the Community Atmosphere
828 Model (CAM5) with in-situ observations, *Atmos. Chem. Phys.*, 14, 10103-10118,
829 10.5194/acp-14-10103-2014, 2014.
- 830 Fusina, F., Spichtinger, P., and Lohmann, U.: Impact of ice supersaturated regions and
831 thin cirrus on radiation in the midlatitudes, *Journal of Geophysical Research:*
832 *Atmospheres*, 112, D24S14, 10.1029/2007JD008449, 2007.
- 833 Gettelman, A., Randel, W. J., Wu, F., and Massie, S. T.: Transport of water vapor in
834 the tropical tropopause layer, *Geophys Res Lett*, 29, 9-1-9-4,
835 10.1029/2001GL013818, 2002.
- 836 Gettelman, A., Liu, X., Ghan, S. J., Morrison, H., Park, S., Conley, A. J., Klein, S. A.,
837 Boyle, J., Mitchell, D. L., and Li, J. L. F.: Global simulations of ice nucleation
838 and ice supersaturation with an improved cloud scheme in the Community
839 Atmosphere Model, *Journal of Geophysical Research: Atmospheres*, 115,
840 D18216, 10.1029/2009JD013797, 2010.
- 841 Gettelman, A., Liu, X., Barahona, D., Lohmann, U., and Chen, C.: Climate impacts of
842 ice nucleation, *Journal of Geophysical Research: Atmospheres*, 117, D20201,
843 10.1029/2012JD017950, 2012.
- 844 Gettelman, A., and Morrison, H.: Advanced Two-Moment Bulk Microphysics for
845 Global Models. Part I: Off-Line Tests and Comparison with Other Schemes, *J*
846 *Climate*, 28, 1268-1287, 10.1175/JCLI-D-14-00102.1, 2015.
- 847 Gettelman, A., Morrison, H., Santos, S., Bogenschutz, P., and Caldwell, P. M.:
848 Advanced Two-Moment Bulk Microphysics for Global Models. Part II: Global
849 Model Solutions and Aerosol-Cloud Interactions, *J Climate*, 28, 1288-1307,
850 10.1175/JCLI-D-14-00103.1, 2015.
- 851 Haag, W., Kärcher, B., Ström, J., Minikin, A., Lohmann, U., Ovarlez, J., and Stohl, A.:
852 Freezing thresholds and cirrus cloud formation mechanisms inferred from in situ
853 measurements of relative humidity, *Atmos. Chem. Phys.*, 3, 1791-1806,
854 10.5194/acp-3-1791-2003, 2003.
- 855 Heymsfield, A. J., Field, P., and Bansemer, A.: Exponential Size Distributions for
856 Snow, *J Atmos Sci*, 65, 4017-4031, 10.1175/2008JAS2583.1, 2008.
- 857 Heymsfield, A. J., Schmitt, C., and Bansemer, A.: Ice cloud particle size distributions
858 and pressure-dependent terminal velocities from in situ observations at
859 temperatures from 0 to -86 C, *J. Atmos. Sci.*, 70, 4123-4154, 2013.
- 860 Hoose, C., and Möhler, O.: Heterogeneous ice nucleation on atmospheric aerosols: a
861 review of results from laboratory experiments, *Atmos. Chem. Phys.*, 12,
862 9817-9854, 10.5194/acp-12-9817-2012, 2012.
- 863 Hoyle, C. R., Luo, B. P., and Peter, T.: The Origin of High Ice Crystal Number
864 Densities in Cirrus Clouds, *J Atmos Sci*, 62, 2568-2579, 10.1175/JAS3487.1,
865 2005.
- 866 Jensen, E. J., Diskin, G., Lawson, R. P., Lance, S., Bui, T. P., Hlavka, D., McGill, M.,
867 Pfister, L., Toon, O. B., and Gao, R.: Ice nucleation and dehydration in the



- 868 Tropical Tropopause Layer, Proceedings of the National Academy of Sciences,
869 110, 2041-2046, 10.1073/pnas.1217104110, 2013.
- 870 Kärcher, B. and Spichtinger, B.: Cloud-controlling factors of cirrus, in: Clouds in the
871 Perturbed Climate System: Their Relationship to Energy Balance, Atmospheric
872 Dynamics, and Precipitation, edited by: Heintzenberg, J. and Charlson, R. J.,
873 Strüngmann Forum Report, 3536, 235–267, The MIT Press, Cambridge, MA,
874 USA, 2009.
- 875 Kay, J. E., Baker, M., and Hegg, D.: Microphysical and dynamical controls on cirrus
876 cloud optical depth distributions, Journal of Geophysical Research: Atmospheres,
877 111, D24205, 10.1029/2005JD006916, 2006.
- 878 Kay, J. E., et al.: Exposing global cloud biases in the Community Atmosphere Model
879 (CAM) using satellite observations and their corresponding instrument
880 simulators, J. Clim., 25, 5190–5207, doi:10.1175/JCLI-D-11-00469.1, 2012.
- 881 Khain, A. P., Beheng, K. D., Heymsfield, A., Korolev, A., Krichak, S. O., Levin, Z.,
882 Pinsky, M., Phillips, V., Prabhakaran, T., Teller, A., van den Heever, S. C., and
883 Yano, J. I.: Representation of microphysical processes in cloud-resolving models:
884 Spectral (bin) microphysics versus bulk parameterization, Rev Geophys, 53,
885 247-322, 10.1002/2014RG000468, 2015.
- 886 Koop, T., Luo, B., Tsias, A., and Peter, T.: Water activity as the determinant for
887 homogeneous ice nucleation in aqueous solutions, Nature, 406, 611-614, 2000.
- 888 Kooperman, G. J., Pritchard, M. S., Ghan, S. J., Wang, M., Somerville, R. C. J., and
889 Russell, L. M.: Constraining the influence of natural variability to improve
890 estimates of global aerosol indirect effects in a nudged version of the Community
891 Atmosphere Model 5, J. Geophys. Res., 117, D23204,
892 doi:10.1029/2012JD018588, 2012.
- 893 Korolev, A. V., Emery, E. F., Strapp, J. W., Cober, S. G., Isaac, G. A., Wasey, M.,
894 and Marcotte, D.: Small Ice Particles in Tropospheric Clouds: Fact or Artifact?
895 Airborne Icing Instrumentation Evaluation Experiment, Bulletin of the American
896 Meteorological Society, 92, 967-973, 10.1175/2010BAMS3141.1, 2011.
- 897 Krämer, M., Schiller, C., Afchine, A., Bauer, R., Gensch, I., Mangold, A., Schlicht, S.,
898 Spelten, N., Sitnikov, N., Borrmann, S., de Reus, M., and Spichtinger, P.: Ice
899 supersaturations and cirrus cloud crystal numbers, Atmos. Chem. Phys., 9,
900 3505-3522, 10.5194/acp-9-3505-2009, 2009.
- 901 Krämer, M., Rolf, C., Luebke, A., Afchine, A., Spelten, N., Costa, A., Meyer, J.,
902 Zöger, M., Smith, J., Herman, R. L., Buchholz, B., Ebert, V., Baumgardner, D.,
903 Borrmann, S., Klingebiel, M., and Avallone, L.: A microphysics guide to cirrus
904 clouds – Part 1: Cirrus types, Atmos. Chem. Phys., 16, 3463-3483,
905 doi:10.5194/acp-16-3463-2016, 2016.
- 906 Lamarque, J. F., Emmons, L. K., Hess, P. G., Kinnison, D. E., Tilmes, S., Vitt, F.,
907 Heald, C. L., Holland, E. A., Lauritzen, P. H., Neu, J., Orlando, J. J., Rasch, P. J.,
908 and Tyndall, G. K.: CAM-chem: description and evaluation of interactive
909 atmospheric chemistry in the Community Earth System Model, Geosci. Model
910 Dev., 5, 369-411, 10.5194/gmd-5-369-2012, 2012.
- 911 Lawson, R. P.: Effects of ice particles shattering on the 2D-S probe, Atmos. Meas.



- 912 Tech., 4, 1361-1381, 10.5194/amt-4-1361-2011, 2011.
- 913 Lebsock, M., Morrison, H., and Gettelman, A.: Microphysical implications of
914 cloud-precipitation covariance derived from satellite remote sensing, *Journal of*
915 *Geophysical Research: Atmospheres*, 118, 6521-6533, 10.1002/jgrd.50347,
916 2013.
- 917 Li, J. L. F., Waliser, D. E., Chen, W. T., Guan, B., Kubar, T., Stephens, G., Ma, H. Y.,
918 Deng, M., Donner, L., Seman, C., and Horowitz, L.: An observationally based
919 evaluation of cloud ice water in CMIP3 and CMIP5 GCMs and contemporary
920 reanalyses using contemporary satellite data, *Journal of Geophysical Research:*
921 *Atmospheres*, 117, D16105, 10.1029/2012JD017640, 2012.
- 922 Liou, K.-N.: Influence of Cirrus Clouds on Weather and Climate Processes: A Global
923 Perspective, *Mon Weather Rev*, 114, 1167-1199,
924 10.1175/1520-0493(1986)114<1167:IOCCOW>2.0.CO;2, 1986.
- 925 Liu, X., and Penner, J. E.: Ice nucleation parameterization for global models,
926 *Meteorol Z*, 14, 499-514, 2005.
- 927 Liu, X., Penner, J. E., Ghan, S. J., and Wang, M.: Inclusion of Ice Microphysics in the
928 NCAR Community Atmospheric Model Version 3 (CAM3), *J Climate*, 20,
929 4526-4547, 10.1175/JCLI4264.1, 2007.
- 930 Liu, X., Easter, R. C., Ghan, S. J., Zaveri, R., Rasch, P., Shi, X., Lamarque, J. F.,
931 Gettelman, A., Morrison, H., Vitt, F., Conley, A., Park, S., Neale, R., Hannay, C.,
932 Ekman, A. M. L., Hess, P., Mahowald, N., Collins, W., Iacono, M. J., Bretherton,
933 C. S., Flanner, M. G., and Mitchell, D.: Toward a minimal representation of
934 aerosols in climate models: description and evaluation in the Community
935 Atmosphere Model CAM5, *Geosci. Model Dev.*, 5, 709-739,
936 10.5194/gmd-5-709-2012, 2012a.
- 937 Liu, X., Shi, X., Zhang, K., Jensen, E. J., Gettelman, A., Barahona, D., Nenes, A., and
938 Lawson, P.: Sensitivity studies of dust ice nuclei effect on cirrus clouds with the
939 Community Atmosphere Model CAM5, *Atmos. Chem. Phys.*, 12, 12061-12079,
940 10.5194/acp-12-12061-2012, 2012b.
- 941 Luebke, A. E., Afchine, A., Costa, A., Groß, J.-U., Meyer, J., Rolf, C., Spelten, N.,
942 Avallone, L. M., Baumgardner, D., and Krämer, M.: The origin of midlatitude
943 ice clouds and the resulting influence on their microphysical properties, *Atmos.*
944 *Chem. Phys.*, 16, 5793-5809, doi:10.5194/acp-16-5793-2016, 2016.
- 945 Mace, G. G., Zhang, Y., Platnick, S., King, M. D., Minnis, P., and Yang, P.:
946 Evaluation of Cirrus Cloud Properties Derived from MODIS Data Using Cloud
947 Properties Derived from Ground-Based Observations Collected at the ARM SGP
948 Site, *Journal of Applied Meteorology*, 44, 221-240, 10.1175/JAM2193.1, 2005.
- 949 Morrison, H., and Gettelman, A.: A New Two-Moment Bulk Stratiform Cloud
950 Microphysics Scheme in the Community Atmosphere Model, Version 3 (CAM3).
951 Part I: Description and Numerical Tests, *J Climate*, 21, 3642-3659,
952 10.1175/2008JCLI2105.1, 2008.
- 953 Morrison, H., and Milbrandt, J. A.: Parameterization of Cloud Microphysics Based on
954 the Prediction of Bulk Ice Particle Properties. Part I: Scheme Description and
955 Idealized Tests. *J. Atmos. Sci.*, 72, 287-311. doi:



- 956 <http://dx.doi.org/10.1175/JAS-D-14-0065.1>, 2015.
- 957 Murphy, D. M., and Koop, T.: Review of the vapour pressures of ice and supercooled
958 water for atmospheric applications, *Quarterly Journal of the Royal*
959 *Meteorological Society*, 131, 1539-1565, 10.1256/qj.04.94, 2005.
- 960 Neale, R. B., and Coauthors: Description of the NCAR Community Atmosphere
961 Model (CAM 5.0), NCAR/TN-486+STR, available at:
962 http://www.cesm.ucar.edu/models/cesm1.0/cam/docs/description/cam5_desc.pdf,
963 2012.
- 964 Park, S., and Bretherton, C. S.: The University of Washington Shallow Convection
965 and Moist Turbulence Schemes and Their Impact on Climate Simulations with
966 the Community Atmosphere Model, *J Climate*, 22, 3449-3469,
967 10.1175/2008JCLI2557.1, 2009.
- 968 Park, S., Bretherton, C. S., and Rasch, P. J.: Integrating Cloud Processes in the
969 Community Atmosphere Model, Version 5, *J Climate*, 27, 6821-6856,
970 10.1175/JCLI-D-14-00087.1, 2014.
- 971 Ramanathan, V., and Collins, W.: Thermodynamic regulation of ocean warming by
972 cirrus clouds deduced from observations of the 1987 El Nino, *Nature*, 351, 27-32,
973 1991.
- 974 Richter, J. H., and Rasch, P. J.: Effects of Convective Momentum Transport on the
975 Atmospheric Circulation in the Community Atmosphere Model, Version 3, *J*
976 *Climate*, 21, 1487-1499, 10.1175/2007JCLI1789.1, 2008.
- 977 Shi, X., Liu, X., and Zhang, K.: Effects of pre-existing ice crystals on cirrus clouds
978 and comparison between different ice nucleation parameterizations with the
979 Community Atmosphere Model (CAM5), *Atmos. Chem. Phys.*, 15, 1503-1520,
980 10.5194/acp-15-1503-2015, 2015.
- 981 Tan, X., Y. Huang, M. Diao, A. Bansemmer, M. A. Zondlo, J. P. DiGangi, R. Volkamer,
982 and Y. Hu: An assessment of the radiative effects of ice supersaturation based on
983 in situ observations, *Geophys. Res. Lett.*, 43, 11,039–11,047,
984 doi:10.1002/2016GL071144, 2016.
- 985 Thayer-Calder, K., Gettelman, A., Craig, C., Goldhaber, S., Bogenschutz, P. A., Chen,
986 C. C., Morrison, H., Höft, J., Raut, E., Griffin, B. M., Weber, J. K., Larson, V. E.,
987 Wyant, M. C., Wang, M., Guo, Z., and Ghan, S. J.: A unified parameterization of
988 clouds and turbulence using CLUBB and subcolumns in the Community
989 Atmosphere Model, *Geosci. Model Dev.*, 8, 3801-3821,
990 10.5194/gmd-8-3801-2015, 2015.
- 991 Wang, M., Ghan, S., Easter, R., Ovchinnikov, M., Liu, X., Kassianov, E., Qian, Y.,
992 Gustafson Jr, W. I., Larson, V. E., Schanen, D. P., Khairoutdinov, M., and
993 Morrison, H.: The multi-scale aerosol-climate model PNNL-MMF: model
994 description and evaluation, *Geosci. Model Dev.*, 4, 137-168,
995 10.5194/gmd-4-137-2011, 2011.
- 996 Wang, M., Liu, X., Zhang, K., and Comstock, J. M.: Aerosol effects on cirrus through
997 ice nucleation in the Community Atmosphere Model CAM5 with a statistical
998 cirrus scheme, *J. Adv. Model. Earth Syst.*, 06, doi:10.1002/2014MS000339,
999 2014.



- 1000 Wang, M. and Penner, J. E.: Cirrus clouds in a global climate model with a statistical
1001 cirrus cloud scheme, *Atmos. Chem. Phys.*, 10, 5449-5474,
1002 doi:10.5194/acp-10-5449-2010, 2010.
- 1003 Wang, P.-H., Minnis, P., McCormick, M. P., Kent, G. S., and Skeens, K. M.: A 6-year
1004 climatology of cloud occurrence frequency from Stratospheric Aerosol and Gas
1005 Experiment II observations (1985–1990), *Journal of Geophysical Research:*
1006 *Atmospheres*, 101, 29407-29429, 10.1029/96JD01780, 1996.
- 1007 Wang, Y., and Liu, X.: Immersion freezing by natural dust based on a soccer ball
1008 model with the Community Atmospheric Model version 5: climate effects,
1009 *Environmental Research Letters*, 9, 124020, 2014.
- 1010 Wofsy, S. C.: HIAPER Pole-to-Pole Observations (HIPPO): fine-grained, global-scale
1011 measurements of climatically important atmospheric gases and aerosols,
1012 *Philosophical Transactions of the Royal Society of London A: Mathematical,*
1013 *Physical and Engineering Sciences*, 369, 2073-2086, 10.1098/rsta.2010.0313,
1014 2011.
- 1015 Wylie, D. P., and Menzel, W. P.: Eight Years of High Cloud Statistics Using HIRS, *J*
1016 *Climate*, 12, 170-184, 10.1175/1520-0442-12.1.170, 1999.
- 1017 Zhang, C., M. Wang, H. Morrison, R. C. J. Somerville, K. Zhang, X. Liu, and J. F. Li
1018 (2014), Investigating ice nucleation in cirrus clouds with an aerosol-enabled
1019 multi-scale modeling framework, *J. Adv. Model. Earth Syst.*, 6, 998–1015,
1020 doi:10.1002/2014MS000343.
- 1021 Zhang, G. J., and McFarlane, N. A.: Sensitivity of climate simulations to the
1022 parameterization of cumulus convection in the Canadian Climate Centre general
1023 circulation model, *Atmosphere-Ocean*, 33, 407-446, 1995.
- 1024 Zhang, K., Liu, X., Wang, M., Comstock, J. M., Mitchell, D. L., Mishra, S., and Mace,
1025 G. G.: Evaluating and constraining ice cloud parameterizations in CAM5 using
1026 aircraft measurements from the SPARTICUS campaign, *Atmos. Chem. Phys.*, 13,
1027 4963-4982, 10.5194/acp-13-4963-2013, 2013.
- 1028 Zhang, K., Wan, H., Liu, X., Ghan, S. J., Kooperman, G. J., Ma, P. L., Rasch, P. J.,
1029 Neubauer, D., and Lohmann, U.: Technical Note: On the use of nudging for
1030 aerosol–climate model intercomparison studies, *Atmos. Chem. Phys.*, 14,
1031 8631-8645, 10.5194/acp-14-8631-2014, 2014.
- 1032 Zondlo, M. A., Paige, M. E., Massick, S. M., and Silver, J. A.: Vertical cavity laser
1033 hygrometer for the National Science Foundation Gulfstream-V aircraft, *Journal*
1034 *of Geophysical Research: Atmospheres*, 115, D20309, 10.1029/2010JD014445,
1035 2010.
- 1036



1037 Table 1. CAM5 experiments

| Experiment name | Nudging | Ice microphysics parameterizations |
|-----------------|------------|---|
| CTL | U, V, T | Threshold diameter for autoconversion of cloud ice to snow (D_{cs}) set to 150 μm |
| DCS75 | U, V, T | As CTL, but with $D_{cs}=75 \mu\text{m}$ |
| DCS300 | U, V, T | As CTL, but with $D_{cs}=300 \mu\text{m}$ |
| SUL | U, V, T | As CTL, but without the lower limit (0.1 μm) for sulfate particle diameter for homogeneous freezing |
| PRE-ICE | U, V, T | As CTL, but with the impacts of pre-existing ice crystals on ice nucleation (Shi et al., 2015) |
| NUG_UV | U, V | As CTL |
| NUG_UVTQ | U, V, T, Q | As CTL |

1038

1039



1040

1041 Table 2. The numbers of cloud occurrences in the 10-second averaged observations
1042 (N_{obs}), as well as those that CAM5 captures (N_{cap}) or misses (N_{mis}) the observed
1043 clouds within the model grid boxes for different temperature ranges. The ratio of N_{cap}
1044 and N_{mis} to N_{obs} are given in parenthesis next to them, respectively.

| Cloud type | Temperature ranges | N_{obs} | N_{cap} | N_{mis} |
|-------------------|--|-----------|---------------|--------------|
| Ice cloud | $T \leq -40^{\circ}\text{C}$ | 3101 | 2925 (94.3%) | 176 (5.7%) |
| Mixed-phase cloud | $-40^{\circ}\text{C} < T \leq 0^{\circ}\text{C}$ | 8768 | 7546 (86.1%) | 1222 (13.9%) |
| Warm cloud | $T > 0^{\circ}\text{C}$ | 3334 | 1665 (49.9%) | 1669 (50.1%) |
| All | | 15203 | 12136 (79.8%) | 3067 (20.2%) |

1045

1046



1047 Table 3. The intercepts and slopes of the regression lines (i.e., $Y=a+b*X$) for dRH_q
 1048 versus dRH , dRH_T versus dRH , and $dRH_{q,T}$ versus dRH in the three experiments CTL,
 1049 NUG_UV, and NUG_UVTQ, respectively. The coefficients are determination (i.e., R^2)
 1050 for each regression line are also presented.

| | | $T \leq -40^\circ\text{C}$ | | | $-40^\circ\text{C} < T \leq 0^\circ\text{C}$ | | | $T > 0^\circ\text{C}$ | | |
|----------|-------------|----------------------------|--------|-------|--|--------|-------|-----------------------|--------|-------|
| | | a | b | R^2 | a | b | R^2 | a | b | R^2 |
| CTL | dRH_q | 5.209 | 0.748 | 0.663 | 4.632 | 0.933 | 0.786 | 0.177 | 0.786 | 0.840 |
| | dRH_T | -0.798 | 0.087 | 0.071 | -3.013 | 0.072 | 0.039 | -0.706 | 0.210 | 0.262 |
| | $dRH_{q,T}$ | -4.411 | 0.165 | 0.241 | -1.619 | -0.005 | .0004 | 0.529 | 0.004 | 0.001 |
| NUG_UV | dRH_q | -16.85 | 0.723 | 0.562 | -5.589 | 0.866 | 0.614 | -5.207 | 0.658 | 0.698 |
| | dRH_T | 29.96 | -0.103 | 0.024 | 10.09 | -0.013 | .0005 | 4.804 | 0.265 | 0.188 |
| | $dRH_{q,T}$ | -13.11 | 0.380 | 0.487 | -4.498 | 0.148 | 0.088 | 0.402 | 0.078 | 0.085 |
| NUG_UVTQ | dRH_q | -2.851 | 0.813 | 0.770 | 2.260 | 0.925 | 0.672 | -1.773 | 0.733 | 0.761 |
| | dRH_T | 3.964 | 0.073 | 0.040 | -0.265 | 0.094 | 0.038 | 1.892 | 0.308 | 0.311 |
| | $dRH_{q,T}$ | -1.113 | 0.114 | 0.262 | -1.996 | -0.019 | 0.003 | -0.119 | -0.041 | 0.095 |

1051

1052



1053

1054 **Figure captions:**

1055 Figure 1. Cloud occurrences simulated by CAM5 (blue and green shaded areas)
1056 compared with HIPPO observations (crosses) during HIPPO#4 Research Flight 05
1057 (H4RF05) from Rarotonga, the Cook Islands (21.2°S, 159.77°W) to Christchurch,
1058 New Zealand (43.48°S, 172.54°E) on June 25–26, 2011. Modeled in-cloud ice crystal
1059 number concentration and cloud droplet number concentration are denoted by blue
1060 and green shaded areas, respectively. Three temperature ranges are used to categorize
1061 the combined measurements of 2DC and CDP probes. The criteria for defining
1062 observed cloud occurrences are described in section 2.

1063 Figure 2. Spatial variabilities of RH, water vapor (Q), and temperature (T) from
1064 CAM5 simulation and HIPPO observation (left), and their differences (right).
1065 Absolute difference between CAM5 and HIPPO is shown for RH and T, while the
1066 ratio between CAM5 and HIPPO is shown for Q. Model performances are denoted by
1067 shaded vertical bars: green (red) denotes when the model captures (misses) the
1068 observed cloud occurrences, and blue denotes when the model simulates a cloud that
1069 is not present in the observation.

1070 Figure 3. As Figure 2a, but for RH recalculated by replacing the model output with
1071 either (a) observed Q or (b) observed T values.

1072 Figure 4. Corresponding (top) dRH_q versus dRH , (middle) dRH_T versus dRH , and
1073 (bottom) $dRH_{q,T}$ versus dRH (unit: %) for different temperature ranges. The colors
1074 indicating three types of model performances in simulating clouds as described in
1075 Fig.2: green (“captured”), red (“missed”) and blue (“overproduced”). The black lines
1076 denote the linear regressions of the samples (i.e., $Y=a+b*X$), and the intercept (i.e., a)
1077 and slope (i.e., b) of the regression lines as well as the coefficient of determination
1078 (i.e., R^2) are shown in the legend.

1079 Figure 5. Observed and simulated probability density functions (PDFs) of relative
1080 humidity with respect to ice (RH_i, unit: %) for $T \leq -40^\circ\text{C}$ separated into clear-sky and
1081 in-cirrus conditions. PDFs of RH_i before and after cloud microphysics in the
1082 simulations are both shown. The RH_i is binned by 2% for the calculation of PDF. The
1083 PDFs (when RH_i>100%) follow an exponent decay: $\ln(\text{PDF})=a+b*\text{RH}_i$. The values
1084 of a and b for each PDF are also shown in dark red (observed), dark blue (simulated
1085 before ice nucleation), and dark green (simulated after cloud microphysics),
1086 respectively. Note blue lines are mostly invisible as overlaid by green lines.



1087 Figure 6. (a-e) Scatterplot of observed versus simulated slope parameter (λ) of the
1088 gamma size distribution function for each experiments, and (f) the frequency of λ for
1089 each range. Note that all the comparisons are restricted to the cases when the model
1090 captures observed ice clouds ($T \leq -40$ °C).

1091 Figure 7. λ versus temperature from the measurements and simulations. The lines are
1092 the geometric mean binned by 4°C, with the vertical bars denoting the geometric
1093 standard deviation. Note that the comparisons are restricted to the cases when the
1094 model captures the observed ice clouds ($T \leq -40$ °C).

1095 Figure 8. As Figure 6, but for the number concentrations (N_i) of ice crystals with
1096 diameters larger than 75 μm for all the experiments. Note that both the comparisons
1097 are restricted to the cases when the model captures observed ice clouds ($T \leq -40$ °C).

1098 Figure 9. As Figure 7, but for N_i .

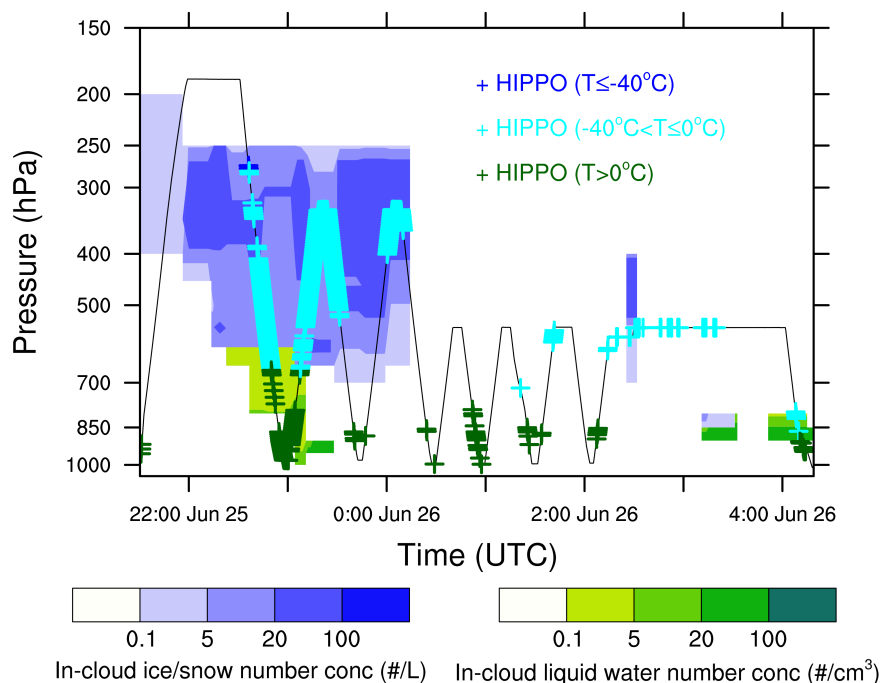
1099 Figure 10. As Figure 8, but for the comparison of ice water content (IWC).

1100 Figure 11. As Figure 9, but for ice water content (IWC) versus temperature.

1101

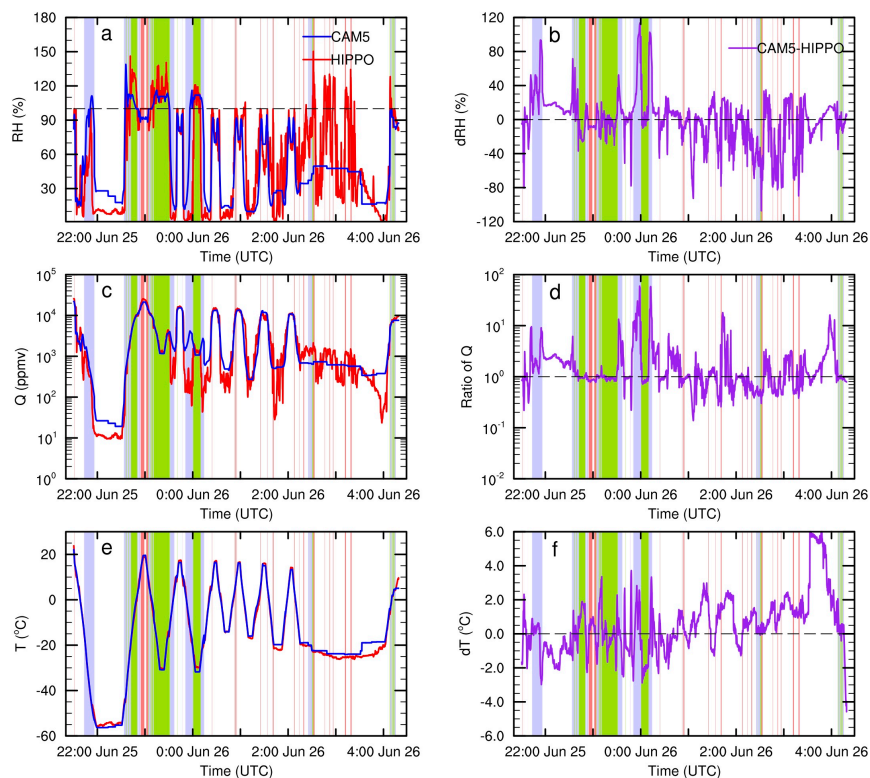


1102



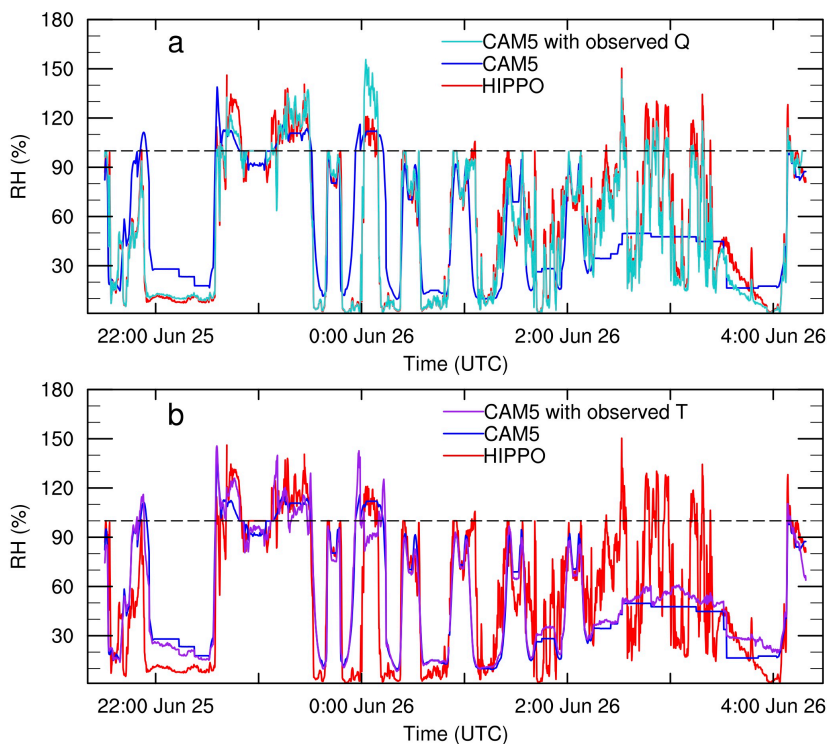
1103

1104 Figure 1. Cloud occurrences simulated by CAM5 (blue and green shaded areas)
1105 compared with HIPPO observations (crosses) during HIPPO#4 Research Flight 05
1106 (H4RF05) from Rarotonga, the Cook Islands (21.2°S, 159.77°W) to Christchurch,
1107 New Zealand (43.48°S, 172.54°E) on June 25–26, 2011. Modeled in-cloud ice crystal
1108 number concentration and cloud droplet number concentration are denoted by blue
1109 and green shaded areas, respectively. Three temperature ranges are used to categorize
1110 the combined measurements of 2DC and CDP probes. The criteria for defining
1111 observed cloud occurrences are described in section 2.



1112

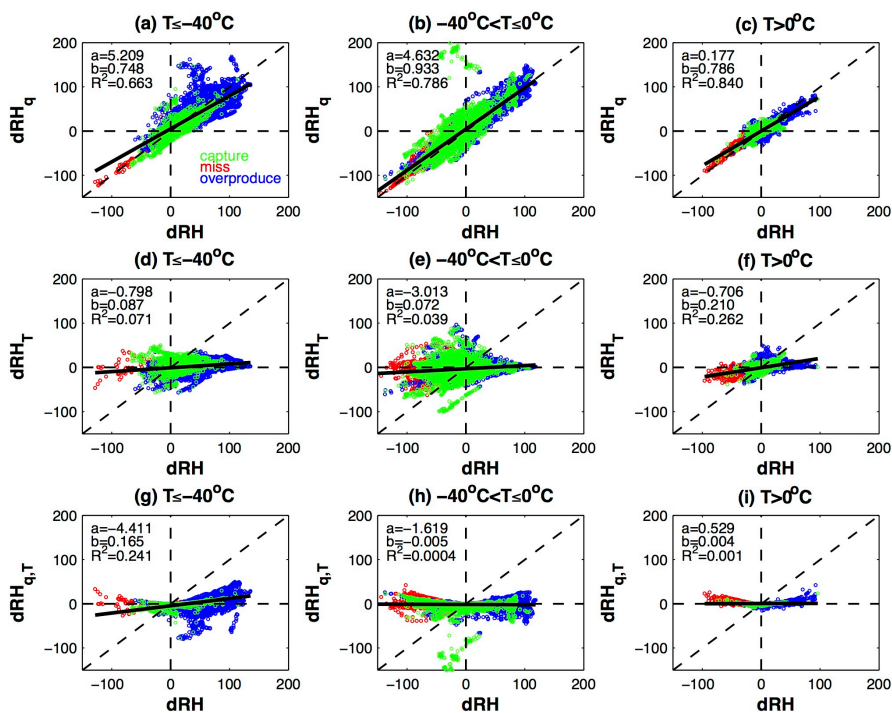
1113 Figure 2. Spatial variabilities of RH, water vapor (Q), and temperature (T) from
1114 CAM5 simulation and HIPPO observation (left), and their differences (right).
1115 Absolute difference between CAM5 and HIPPO is shown for RH and T, while the
1116 ratio between CAM5 and HIPPO is shown for Q. Model performances are denoted by
1117 shaded vertical bars: green (red) denotes when the model captures (misses) the
1118 observed cloud occurrences, and blue denotes when the model simulates a cloud that
1119 is not present in the observation.



1120

1121 Figure 3. As Figure 2a, but for RH recalculated by replacing the model output with
 1122 either (a) observed Q or (b) observed T values.

1123



1124

1125 Figure 4. Corresponding (top) dRH_q versus dRH , (middle) dRH_T versus dRH , and
 1126 (bottom) $dRH_{q,T}$ versus dRH (unit: %) for different temperature ranges. The colors
 1127 indicating three types of model performances in simulating clouds as described in
 1128 Fig.2: green (“captured”), red (“missed”) and blue (“overproduced”). The black lines
 1129 denote the linear regressions of the samples (i.e., $Y = a + b \cdot X$), and the intercept (i.e., a)
 1130 and slope (i.e., b) of the regression lines as well as the coefficient of determination
 1131 (i.e., R^2) are shown in the legend.

1132

1133

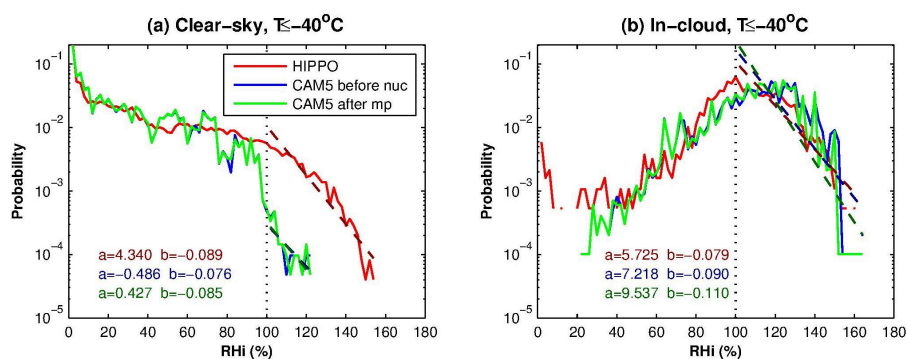
1134

1135

1136



1137



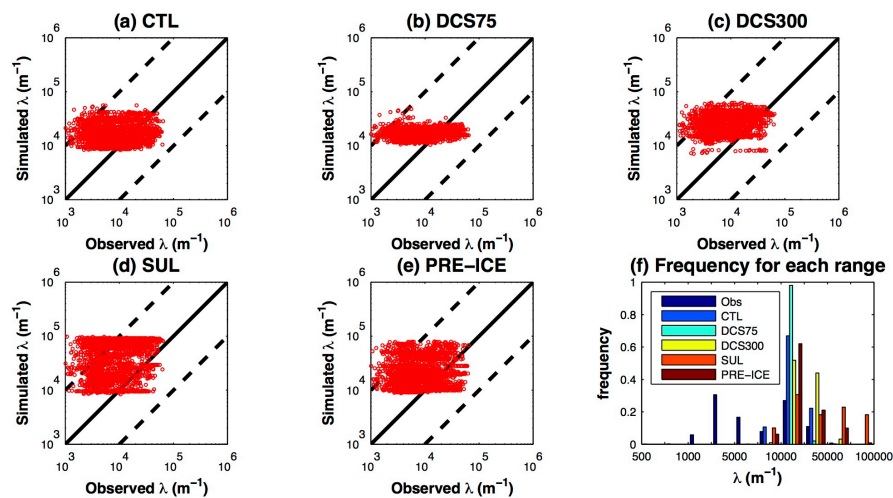
1138

1139 Figure 5. Observed and simulated probability density functions (PDFs) of relative
1140 humidity with respect to ice (RH_i , unit: %) for $T \leq -40^\circ\text{C}$ separated into clear-sky and
1141 in-cirrus conditions. PDFs of RH_i before and after cloud microphysics in the
1142 simulations are both shown. The RH_i is binned by 2% for the calculation of PDF. The
1143 PDFs (when $RH_i > 100\%$) follow an exponent decay: $\ln(\text{PDF}) = a + b \cdot RH_i$. The values
1144 of a and b for each PDF are also shown in dark red (observed), dark blue (simulated
1145 before ice nucleation), and dark green (simulated after cloud microphysics),
1146 respectively. Note blue lines are mostly invisible as overlaid by green lines.
1147



1148

1149



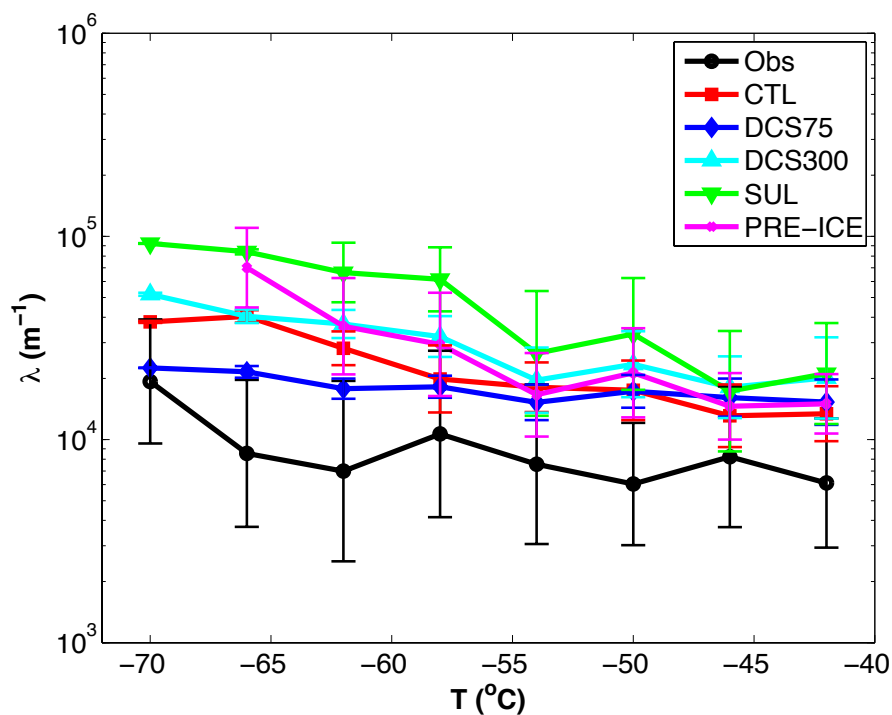
1150

1151 Figure 6. (a-e) Scatterplot of observed versus simulated slope parameter (λ) of the
1152 gamma size distribution function for each experiments, and (f) the frequency of λ for
1153 each range. Note that all the comparisons are restricted to the cases when the model
1154 captures observed ice clouds ($T \leq -40$ °C).

1155



1156



1157

1158 Figure 7. λ versus temperature from the measurements and simulations. The lines are
1159 the geometric mean binned by 4°C, with the vertical bars denoting the geometric
1160 standard deviation. Note that the comparisons are restricted to the cases when the
1161 model captures the observed ice clouds ($T \leq -40$ °C).

1162

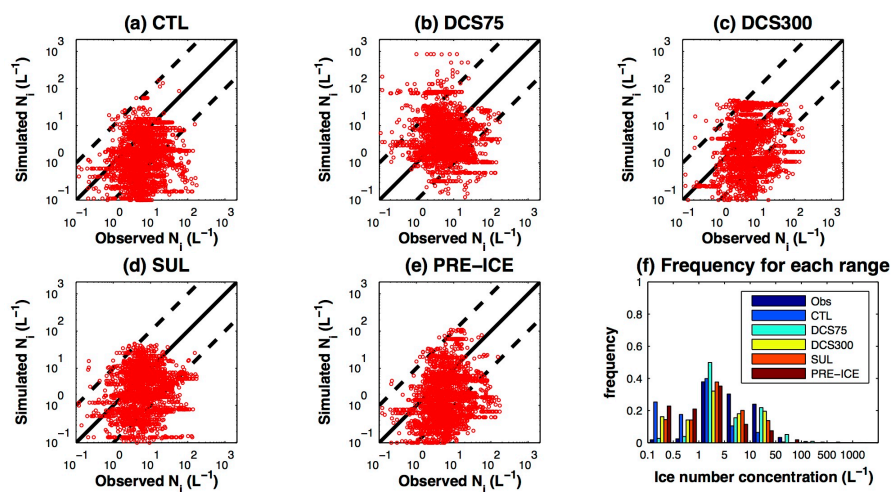
1163

1164

1165

1166

1167



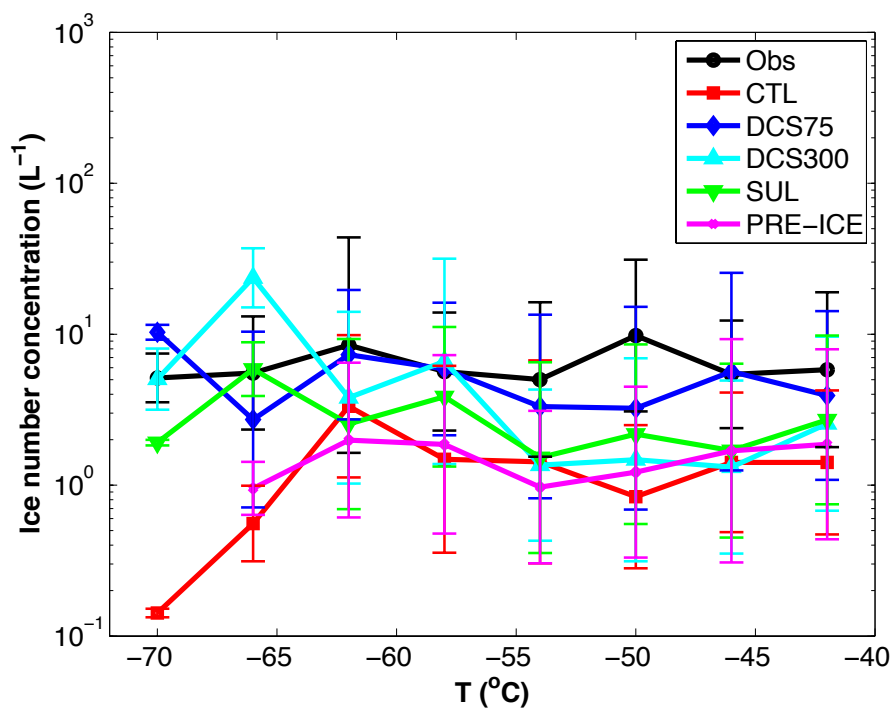
1168

1169 Figure 8. As Figure 6, but for the number concentrations (N_i) of ice crystals with
1170 diameters larger than $75 \mu m$ for all the experiments. Note that both the comparisons
1171 are restricted to the cases when the model captures observed ice clouds ($T \leq -40 \text{ }^\circ C$).

1172



1173



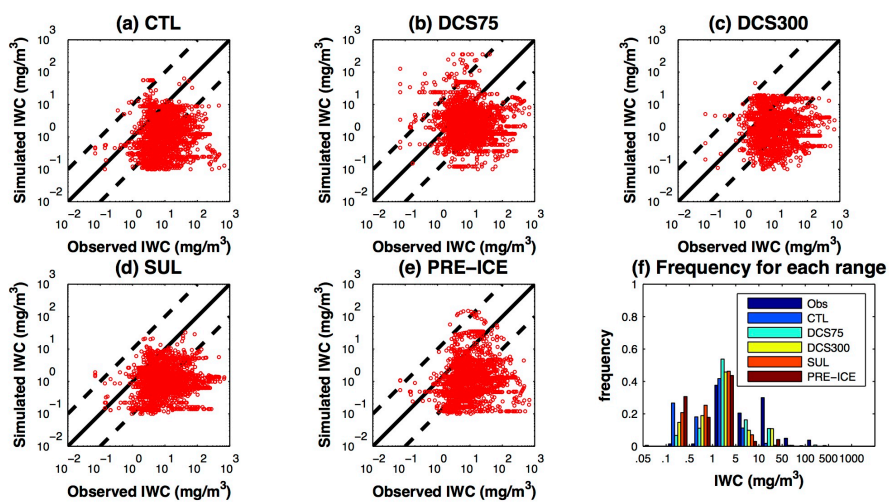
1174

1175 Figure 9. As Figure 7, but for N_i .

1176



1177



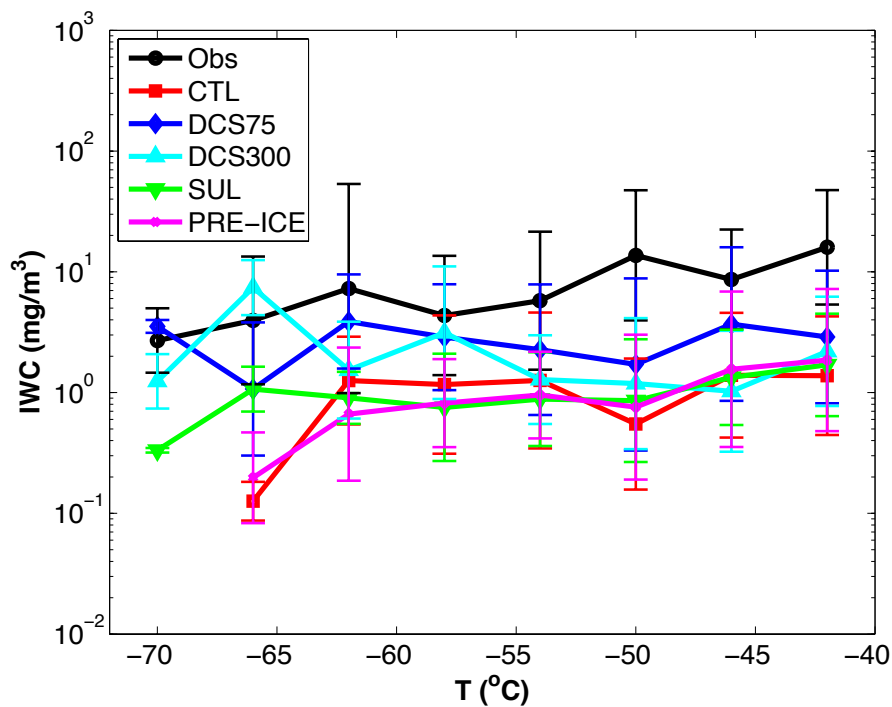
1178

1179 Figure 10. As Figure 8, but for the comparison of ice water content (IWC).

1180



1181



1182

1183 Figure 11. As Figure 9, but for ice water content (IWC) versus temperature.

1184